



Designing a smart heterojunction coupling of cobalt-iron layered double hydroxide on nickel selenide nanosheets for highly efficient overall water splitting kinetics

Shrine Maria Nithya Jeghan^{a,1}, Dongjoon Kim^{b,1}, Yuhyeon Lee^a, Minkyu Kim^{a,*}, Gibaek Lee^{a,*}

^a School of Chemical Engineering, Yeungnam University, 38541 Gyeongsan, Republic of Korea

^b William G. Lowrie, Department of Chemical and Biomolecular Engineering, 422 CBEC, 151 W Woodruff Ave, Columbus, OH 43210, United States

ARTICLE INFO

Keywords:

Heteronanostructures
Interfacial coupling
Oxygen evolution reaction
Hydrogen evolution reaction
Water splitting

ABSTRACT

To design heterojunction electrocatalysts for water splitting in industrial plants, replacing RuO₂, IrO₂, and Pt/C remains challenging. We prepared heterostructures of nickel selenide (NiSe) and cobalt-iron layer double hydroxide (CoFe-LDH), CoFe-LDH@NiSe, using hydrothermal and electrodeposition processes. The interfacial coupling enhanced the oxygen evolution reaction (OER) and the hydrogen evolution reaction (HER). The CoFe-LDH@NiSe required an overpotential of 127 mV and 38 mV for a current density of 10 mA cm⁻² with a Tafel slope of 37 mV dec⁻¹ and 33 mV dec⁻¹ for OER and HER in alkaline solutions. Density functional theory calculations showed the enhancement of OER performance. The catalytic activity of CoFe-LDH@NiSe increased the electronic conductivity, enhancing the water splitting with 10 mA cm⁻² at 1.51 V. The robustness was demonstrated by the long-term stability for 120 h. This study provides a strategy for developing heteronanostructure electrocatalysts for water splitting in fields such as metal-air batteries and energy storage.

1. Introduction

With depleting resources of fossil fuels and the growing demand for renewable resources, it is essential to develop sustainable energy for a greener world. Hydrogen has high energy density, is a source of clean energy, and causes no harm to the environment; thus, it is considered a next-generation energy carrier [1]. In the last few decades, H₂ has been produced using various strategies such as steam reforming, coal gasification, partial oxidation of methane, and photocatalytic and electrocatalytic water splitting [2–4]; however, it is still primarily produced by the steam reforming process. However, this process is limited because it requires high temperatures and produces excessive CO₂ emissions [5]. To address these issues, electrocatalytic water splitting via electrolysis has considerable potential to produce clean H₂ with zero carbon emissions [6]. The overall water splitting electrolysis can be divided into two

half-cell reactions: the anodic oxygen evolution reaction (OER) and the cathodic hydrogen evolution reaction (HER) [7]. Both reactions are slow and catalysts are required to overcome the potential energy barrier to produce hydrogen and oxygen. However, the critical bottleneck lies in the OER as it involves a four-electron transfer process, which requires a higher overpotential than that of the HER [8,9]. As of now, Ir and Ru oxides or doped transition metal oxides and Pt show better activity for delivering benchmark current density (10 mA cm⁻²) for the OER and the HER [10–14]. However, poor stability and high cost are drawbacks for large-scale industrial applications. Therefore, a highly conductive, inexpensive, and stable electrocatalyst is favorable for the reduction of overpotential with high current density.

To meet these challenges, researchers have focused on designing non-precious electrocatalysts based on hydroxides, layer double hydroxide, oxides, sulfides, selenides, phosphides, nitrides, and carbides of

Abbreviations: LDHs, layer double hydroxides; OER, oxygen evolution reaction; HER, hydrogen evolution reaction; DFT, density functional theory; NF, nickel foam; XRD, X-ray diffraction; FE-SEM, field-emission scanning transmission microscopy; EDS, Energy Dispersive X-ray Spectroscopy; SAED, selected area electron diffraction; HR-TEM, high-resolution transmission electron microscopy; STEM-HAADF, scanning transmission electron microscopy-high angular annular dark field; XPS, X-ray photoelectron spectroscopy; LSV, linear sweep voltammetry; CV, cyclic voltammetry; EIS, electrochemical impedance spectroscopy; VASP, Vienna ab initio simulation package; ECSA, electrochemical active areas; CA, chronoamperometry.

* Corresponding authors.

E-mail addresses: mk_kim@ynu.ac.kr (M. Kim), gibaek@ynu.ac.kr (G. Lee).

¹ These authors contributed equally to this work

<https://doi.org/10.1016/j.apcatb.2022.121221>

Received 7 December 2021; Received in revised form 3 February 2022; Accepted 12 February 2022

Available online 15 February 2022

0926-3373/© 2022 Elsevier B.V. All rights reserved.

transition metals such as V, Mo, W, Fe, Co, and Ni. These electrocatalysts show high activities due to their highly conductive nature, more active sites, mass charge transfer, and synergistic effects on water electrolysis [15–18]. Among these, metal chalcogenides are the most attractive electrocatalysts due to their low cost, high stability, and better electrocatalytic performance than simple oxides/hydroxides [19]. Selenide with the electronic structure $4s^2p^4$ and empty $3d$ orbitals leads to the formation of strong metallic bonds with transition metals, which is beneficial for electron transport in water electrolysis [20]. In particular, the electronic conductivity of selenium ($1 \times 10^{-3} \text{ S m}^{-1}$) is higher than that of sulfur ($5 \times 10^{-28} \text{ S m}^{-1}$) [21,22]. In this context, metal selenides such as monometallic selenides (CoSe, NiSe, MoSe₂), bimetallic selenides (NiCo₂Se₄, Ni_xFe_{1-x}Se₂, Co_xFe_{1-x}Se₂, Ni_xMo_{1-x}Se₂), and multi-metal selenides (Fe–Cu–Co–Se, Co–Ni–Cu–Se) are promising non-noble electrocatalysts for water splitting [23–27]. Moreover, compared to binary/multimetal selenides, monometallic metal selenides reduce the complexity of the catalysis system and simplify the synthesis process [28]. Nickel selenides exist in the forms of NiSe, Ni_{0.85}Se, NiSe₂, Ni₃Se₂, and Ni₃Se₄, which are important compounds due to their extensive OER and HER activities [29,30].

With this understanding, nickel selenides are a good choice as electrocatalysts for the overall water splitting process. However, the limitation of transition metal selenides is their deficient active sites [31]. To overcome this setback, engineering these metal selenides to boost the catalytic activity increases the number of active sites. Additionally, there are possible synergistic effects between the two side electrocatalysts by partial delocalization of electrons at the interface through oxygen bridging [32]. Because of the increased catalytic activity, promising electrocatalyst layer double hydroxides (LDHs) have attracted attention and have the additional characteristics of special 2D structure with large surface areas, tunable compositions, low earth abundance, and abundant active sites [33]. Typically, transition-metal-based LDHs have potential strength for OER and HER electrocatalysts [34]. In particular, bimetallic LDH materials such as NiFe–LDH, NiCo–LDHs, CoFe–LDH, and CoMo–LDH have been exclusively studied for water splitting [35–39]. However, they suffer from low conductivity, which limits the water dissociation process. Nevertheless, their catalytic properties can be improved by the heterostructure interface, thereby enhancing the charge, and leading to better contact between the electrolyte and catalyst [40]. NiFe–LDH based heterostructure electrocatalysts like CoSe/NiFe–LDH, Co₃O₄@NiFe–LDH/nickel foam (NF), NiFe–LDH–NiSe/NF, V–Ni₃S₂@NiFe–LDH, and NiFe–LDH@NiCoP/NF show excellent activity in water splitting [32,41–44]. CoFe–LDH competitive with NiFe–LDH has excellent characteristic features with the presence of both Co and Fe ions in the host layers, which can provide abundant redox reactions during the electrochemical processes. However, few reports are available for CoFe/NiFe–LDH/NF, CeO_{2-x}@CoFe LDH/NF, and CuO@CoFe–LDH/CF [33,45,46]. Based on these results, NiSe, which is highly conductive in nature with deficient active sites, and CoFe–LDH, which has abundant active sites but poor conductivity, could be beneficial for enhancing their electrocatalytic properties. Earlier works with a designed architecture showed excellent electrocatalytic performance for overall water splitting.

In this study, a hierarchical heterostructure of CoFe–LDH@NiSe on NF was successfully prepared through hydrothermal and electrodeposition methods. First, nickel hydroxide prepared by the hydrothermal route was converted to nickel selenide via selenization and hierarchical CoFe–LDH nanosheets were electrodeposited on NiSe nanosheets. The prepared CoFe–LDH@NiSe nanosheets showed remarkable electrocatalytic activity toward the overall water splitting process. Density functional theory (DFT) calculations revealed that the integrated CoFe–LDH@NiSe surface optimized the OER intermediate adsorption energies. Furthermore, the synergy between NiSe and CoFe–LDH was supported by the experimental findings confirming that the interfacing CoFe–LDH@NiSe electrocatalyst is endowed with superior OER and HER performance, which yields one of the highest catalytic activities.

Particularly, the designed electrocatalyst demonstrates efficient water splitting in a two-electrode system with a cell voltage as low as 1.51 V for 10 mA cm⁻² current density in an alkaline medium with outstanding long-term stability for 5 days. This superior performance was attributed to the sheet-like heterostructure of CoFe–LDH and NiSe for the following reasons: (1) CoFe–LDH provided massive exposed active sites and interconnected mass electron charge transfer; (2) NiSe sites provided the catalyst conductivity, benefiting OH adsorption between the catalyst and electrolyte interfaces; (3) the combination of Ni, Co, and Fe generated rich active sites to promote the adsorption of hydroxide and protons. This study provides novel insights into the design of low-cost and durable electrocatalysts for water splitting.

2. Experimental section

2.1. Materials

Nickel (II) nitrate hexahydrate (Ni(NO₃)₂·6H₂O), cobalt (II) nitrate hexahydrate (Co(NO₃)₂·6H₂O), iron (II) sulfate heptahydrate (FeSO₄·7H₂O), sodium selenite (Na₂SeO₃), urea (NH₂CONH₂), ammonium fluoride (NH₄F), and hydrazine (N₂H₄) were purchased from Sigma Aldrich. All chemicals were used without further purification. NF, ethanol, and potassium hydroxide (KOH) were obtained from Duskan Pure Chemicals Co., Ltd. Deionized (DI) water was used throughout the experiments.

2.2. Synthesis of sheet-like NiSe on nickel foam (NF)

NiSe sheets on NF were synthesized via a two-step hydrothermal reaction. Ni(OH)₂ was prepared by dissolving 50 mM of Ni(NO₃)₂·6H₂O, 250 mM NH₂CONH₂, and 125 mM NH₄F in 20 mL of DI water and stirring for 15 min to form a homogeneous solution. Then, the above solution was transferred into a 50 mL Teflon-lined stainless steel autoclave and NF (1 × 3 cm²) cleaned with acetone was heated to 120 °C for 12 h. After cooling to room temperature, the NF was removed, washed with DI water to remove residues, and then dried overnight at 70 °C. Thereafter, 0.1 g Na₂SeO₃ was dissolved in 20 mL DI water and 1 mL N₂H₄ was added dropwise; the clear solution was transferred to a 50 mL Teflon-lined stainless steel autoclave. The NF was then heated at 120 °C for 12 h, after which it was removed, rinsed with DI water and ethanol, and dried at 70 °C. The calculated average mass loading on NF was ~2.02 mg cm⁻².

2.3. Synthesis of hierarchical heterostructure of CoFe–LDH@NiSe

Hierarchical CoFe–LDH sheets were grown on the surface of the NiSe substrate via electrodeposition. The fabrication of CoFe–LDH was carried out on a three-electrode glass cell, where NiSe/NF was directly used as a working electrode and a platinum sheet and an Ag/AgCl electrode were used as the counter and reference electrodes, respectively. In a typical process, 25 mM Co(NO₃)₂·6 H₂O and 25 mM FeSO₄·7 H₂O dissolved in 100 mL DI water were used as electrolyte solutions. The CoFe–LDH sheet-like structure was electrodeposited with constant potential of –1.0 V for 100 s. The formed CoFe–LDH@NiSe was rinsed with water and ethanol and dried overnight at 70 °C. The average mass loading calculated on NF was ~2.15 mg cm⁻². For comparison, CoFe–LDH sheets were directly electrodeposited on NF (working electrode) under the same experimental conditions. The mass loading was calculated to be ~2.07 mg cm⁻² (surface area = 1 cm × 1 cm).

2.4. Preparation of commercial electrocatalysts RuO₂, IrO₂ and Pt/C-supported NF

For a comparative study, samples such as RuO₂, IrO₂, and Pt/C purchased from Sigma Aldrich were used to evaluate the OER and the HER performances of the as-synthesized materials. Briefly, 5 mg of each

catalyst powder was mixed with isopropyl alcohol, DI water, and 5 wt% Nafion solution, and then sonicated for 30 min. The ink solution was then coated onto the NF and dried in a hot air oven. The loading mass of the active catalysts was calculated to be $\sim 2.0 \text{ mg cm}^{-2}$.

2.5. Characterization techniques

The crystallographic information of the as-prepared materials was examined using X-ray diffraction (XRD, X'pert Pro, PANalytical diffractometer) equipped with a nickel-filtered $\text{Cu-K}\alpha$ radiation source (40 kV, 30 mA, 1.54051 \AA). The morphology of the samples was characterized using field-emission scanning transmission microscopy (FE-SEM; S-4800, HITACHI). The detailed structural features, lattice spacing, selected area electron diffraction (SAED) pattern, and elemental composition were observed using high-resolution transmission electron microscopy (HR-TEM) and scanning transmission electron microscopy-high angular annular dark field (STEM-HAADF, FEI Tecnai G2 F20 instrument with an accelerating voltage of 200 kV. X-ray photoelectron spectroscopy (XPS) measurements were recorded using ESCALAB 250 instrument to explore the elemental surface composition of the samples. In particular, the heterostructure formation of CoFe-LDH@NiSe was evaluated using a micro-Raman spectrophotometer (XploRA, Horiba) using an Ar^+ laser (532 nm) at the Core Research Support Center for Natural Products and Medical Materials at Yeungnam University.

2.6. Electrochemical measurements

All electrochemical measurements were conducted on an Autolab potentiostat galvanostat (PGSTAT 302 N, Metrohm, Eco-chemie, Utrecht, the Netherlands) equipped with three-electrode glass cells. In a typical setup, NiSe, CoFe-LDH, and CoFe-LDH@NiSe catalyst supported on NF, the Pt plate, and Ag/AgCl electrode, were used as the working electrode, counter and the reference electrodes, respectively. All linear sweep voltammetry (LSV) curves were recorded at a scan rate of 5 mVs^{-1} . The LSV curves for the OER and the HER were recorded within potential ranges of 1.1–1.8 V and between -0.1 and -0.8 V vs. RHE, respectively. The measured potentials were calibrated to a RHE using the Nernst Eq. 1:

$$E_{\text{RHE}} = E_{\text{Ag/AgCl}} + E^0_{\text{Ag/AgCl}} + 0.059 \text{ pH} \quad (1)$$

The double-layered capacitance was estimated under a non-faradic region by measuring the capacitive current associated with double-layer charging, calculated from the different cyclic voltammetry (CV) scan rates for the OER and the HER. The long-term stability of the electrocatalyst was checked via chronopotentiometry and amperometry techniques at a constant current density of 20 mA cm^{-2} . Electrochemical impedance spectroscopy (EIS) analysis was carried out in the frequency range of 100 kHz to 1 Hz with an amplitude of 10 mV for the OER and the HER. The overall water splitting activity of NiSe, CoFe-LDH, and CoFe-LDH@NiSe in 1.0 M KOH was measured in a two-electrode configuration, where each individual catalyst was used as both the cathode and the anode in a closed electrochemical cell.

2.7. Theoretical calculation methods

DFT calculations were performed using projector augmented wave pseudopotentials provided in the Vienna ab initio simulation package (VASP) [47,48]. The Perdew-Burke-Ernzerhof exchange-correlation with Hubbard U corrections were used with a plane wave expansion cutoff of 600 eV and 400 eV for bulk and surface, respectively; U values are 3.3 eV for Co, 4.3 eV for Fe and 6.45 eV for Ni [49–54]. In addition, we employed spin-polarized calculations and water solvation corrections to stabilize OOH^* (0.25 eV) and OH^* (0.5 eV) [55]. The space groups of P-63/mmc (NiSe) and the α phase CoFe-LDH with

three-layered rhombohedral structure were used to relax the bulk lattice constants until the forces reached at least 0.01 eV/\AA with Monkhorst-Pack k-points mesh $6 \times 8 \times 4$ (CoFe-LDH) and $8 \times 8 \times 8$ (NiSe) [56]. For the slab calculations, we used a $2 \times 2 \times 1$ k-point mesh for all slab systems in this study. The PBE+U relaxed bulk lattice constants of NiSe ($a = b = 3.65 \text{ \AA}$, $c = 5.24 \text{ \AA}$); CoFe-LDH ($a = 12.59 \text{ \AA}$, $b = 6.28 \text{ \AA}$, $c = 23.09 \text{ \AA}$) were used to fix the lateral dimensions of NiSe and CoFe-LDH slabs. The NiSe and CoFe-LDH surfaces had 2×2 and 1×2 surface unit cell sizes of $\sim 8 \text{ \AA}$ and $\sim 12 \text{ \AA}$, respectively. The NiSe (110) plane consisted of five layers with the bottom 3 layers fixed, and the CoFe-LDH surface was made of two CoFe-LDH layers with a fixed bottom layer [57,58]. The other non-fixed surface layers were allowed to relax until the forces were below 0.05 eV/\AA . In terms of the CoFe-LDH@NiSe surface, the (110) facet of the NiSe lattice was well fit with the CoFe-LDH surface lattice. More details and additional information on the computational settings can be found in the [Supporting Information](#).

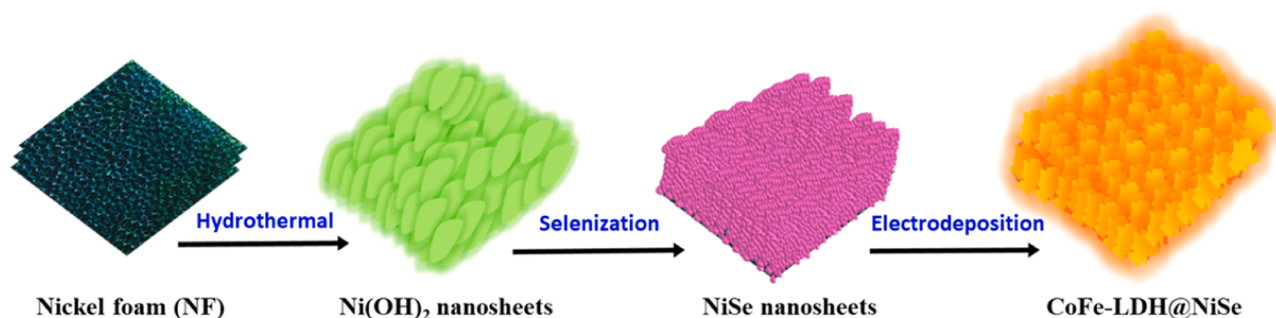
3. Results and discussion

3.1. Morphological features of NiSe and CoFe-LDH@NiSe

Scheme 1 illustrates the fabrication process of CoFe-LDH coupled with NiSe on NF via hydrothermal and electrodeposition routes. In the first step, Ni(OH)_2 nanosheets were prepared on the NF through a hydrothermal method. The green color of $\beta\text{-Ni(OH)}_2$ nanosheets on the NF is due to the weak oxidation reaction of Ni in water, as reported in the literature [59]. In the second step, Ni(OH)_2 was converted to NiSe nanosheets by an anion exchange reaction in which the inner Ni(OH)_2 diffused out, while the Se^{2-} ions diffused inward on the surface of the nanosheets. In brief, Na_2SeO_3 was reduced to Se^{2-} ions; subsequently, Ni was oxidized to Ni^{2+} , forming a tetra-amine nickel $[\text{Ni}(\text{NH}_3)_4]^{2+}$ complex with $\text{N}_2\text{H}_4 \cdot 2 \text{H}_2\text{O}$ aqueous solution. Therefore, this reaction led to the formation of black-colored NiSe nanosheets [60]. Finally, the electrodeposition method was used to grow CoFe-LDH nanosheets on the surface of the NiSe nanosheets, forming a CoFe-LDH@NiSe heterostructure with a pinkish black color.

To study the structural transformation of Ni(OH)_2 to CoFe-LDH@NiSe heteronanostructures, we investigated the morphological changes using field-emission scanning electron microscopy (FE-SEM). Fig. 1a₁–a₃ shows the low- and high-resolution images of well-aligned, highly dense Ni(OH)_2 nanosheets with a smooth surface. The EDS spectra and elemental mapping images confirm the uniform distribution of Ni and O (Fig. S1a–d). However, the surface of the NiSe nanosheets changed to a rough surface, indicating the formation of NiSe nanoparticles, suggesting the replacement of OH^- ions by Se^{2-} ions (Fig. 1b₁–b₃). The nanoparticles were interconnected to form network-like structures, and their corresponding EDS and elemental mapping depict the presence of intermixed Ni and Se (Fig. S1e–h). Compared to the structures of Ni(OH)_2 and NiSe, the CoFe-LDH@NiSe morphology is unique. Featherlike structures such as CoFe-LDH nanosheets can be clearly observed from the covering surface of NiSe nanosheets. A core-shell architecture (Fig. 1c₁–c₃) is believed to promote OER and HER activities through surface engineering, increasing the conductivity and active sites. The EDS spectrum and elemental mapping show the uniform distribution of Ni, Se, Co, Fe, and O (Fig. S1i–o). Pristine CoFe-LDH nanosheets on NF exhibit dense how tiny such as 1–2 nm that are interconnected to form a porous skeleton-like sheets beneficial to provide more active sites (Fig. S2a–c).

The CoFe-LDH@NiSe and NiSe nanosheets were further examined using TEM. Fig. 2a and b show the TEM and HR-TEM images of as-prepared CoFe-LDH@NiSe nanosheets, where CoFe-LDH sheets covered the NiSe forming core-shell like nanostructures. They are interconnected with each other, providing fast electrolyte diffusion and gas release (Fig. 2b) [43]. The SAED patterns clearly show the reflections of the (003), (006), (012), (015), and (018) planes of the CoFe-LDH



Scheme 1. Schematic illustration of the structure and heterojunction coupling of CoFe-LDH@NiSe through hydrothermal and electrodeposition process.

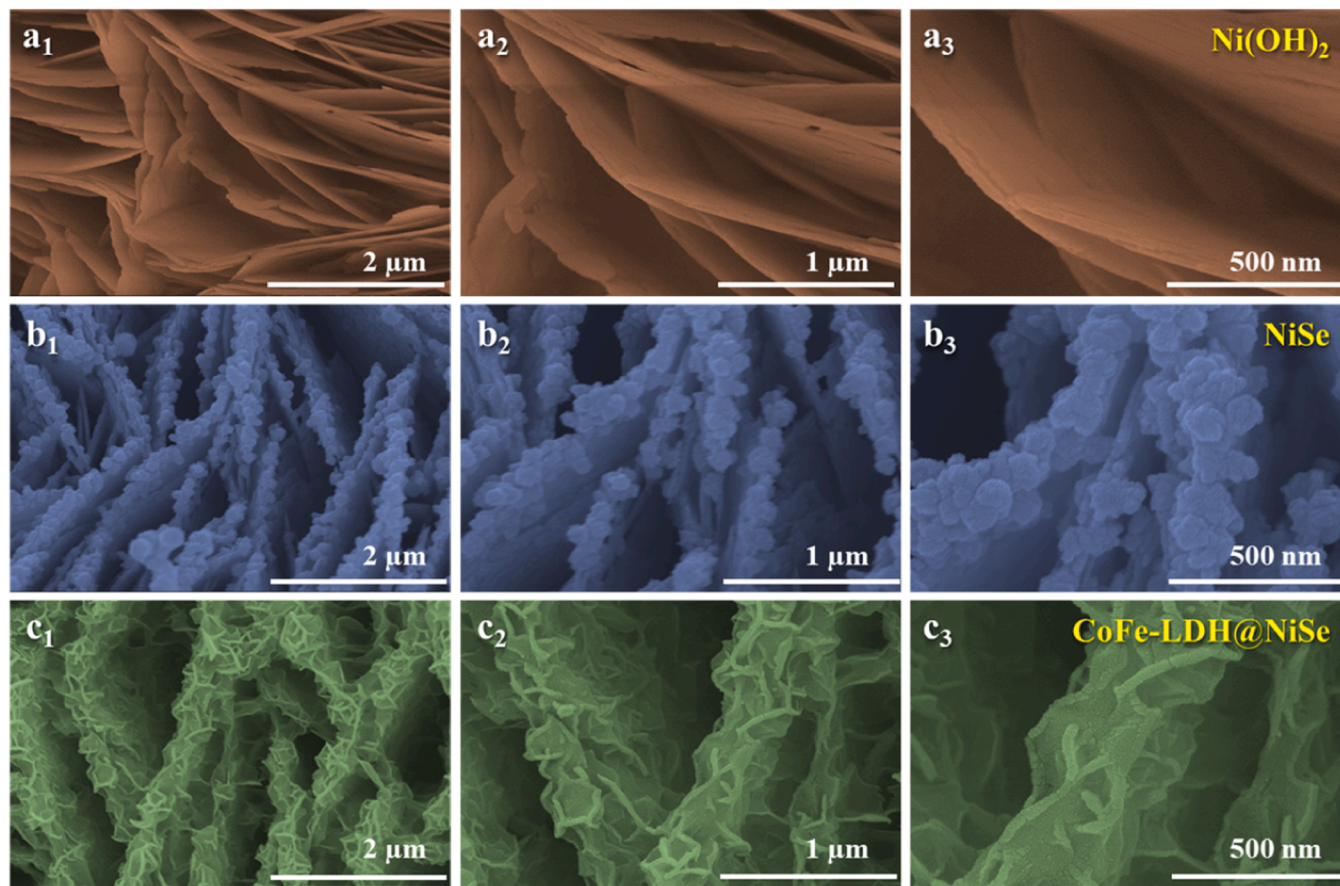


Fig. 1. Low- and high-magnification FE-SEM images of (a₁–a₃) Ni(OH)₂ nanosheets, (b₁–b₃) NiSe nanosheets, and (c₁–c₃) CoFe-LDH@NiSe nanosheets.

sheets, respectively. The HR-TEM image shows defects in CoFe-LDH nanosheets marked by arrows (Fig. 2d), suggesting the existence of extensive defects and disordered lattice dislocations. These defects increase the number of exposed active sites and change the electronic properties of the interface, dramatically improving the catalytic activity [61]. In addition, Fig. 2e clearly depicts the heterointerfaces and lattice fringes with *d*-spacing of 0.20 nm for (102) plane and 0.23 nm for (015) plane corresponding to NiSe and CoFe-LDH sheets, respectively. In addition, defects in the CoFe-LDH nanosheets can also be observed (marked by arrows). The bright field image and HAADF images show the even distribution of Ni, Se, Co, Fe, and O elements (Fig. 2 f). The EDS point line results and spectrum further confirm the elemental composition with atomic percentages of 21.99% (Ni), 22.21% (Se), 11.41% (Co), 10.21% (Fe), and 34.31% (O), respectively (Fig. S3), where the high oxygen content confirms the formation of LDH with high oxygen vacancies. Furthermore, TEM and HR-TEM images of the NiSe

nanosheet show well-formed clear thick sheets, which indicate that the porous voids (holes) present in the sheets are marked by green circles (Fig. S4a, b). These sheets are made up of several nanoparticles that are united to form a network of sheet-like structures. The HR-TEM image shows lattice fringes with *d*-spacing of 0.27 nm corresponding to the (101) plane of NiSe (Fig. S4c). The SAED pattern shows the diffraction patterns of the (100), (101), (102), (110), and (103) crystallographic planes of the as-prepared NiSe nanosheets (Fig. S4d). The bright field images and HAADF-STEM images reveal the uniform distribution of Ni and Se in the NiSe nanosheets (Fig. S4e). The EDS line scanning results and spectrum also confirmed the evenly dispersed Ni (49.52%) and Se (50.48%) elements in a 1:1 ratio (Fig. S4f and g).

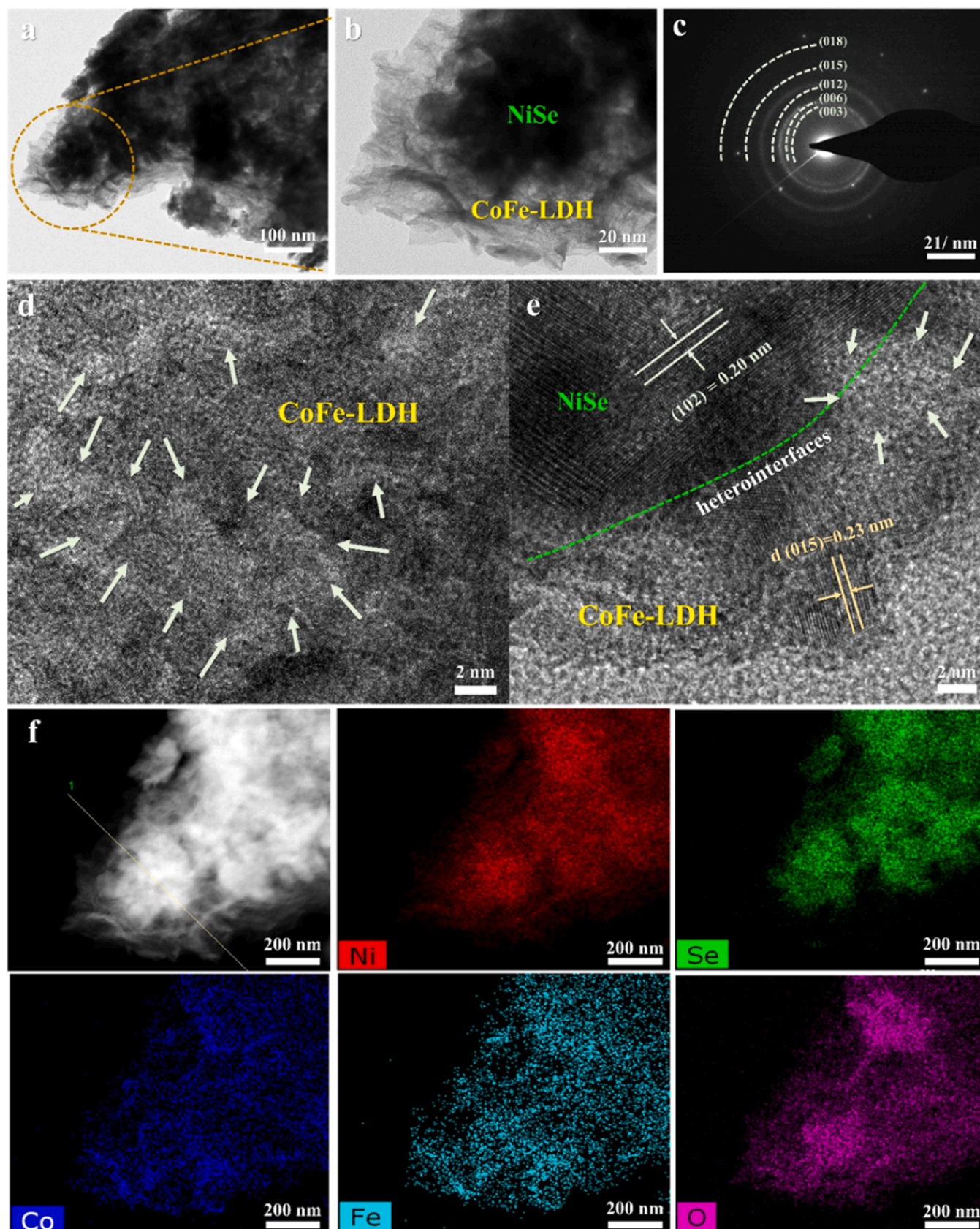


Fig. 2. (a and b) TEM images, (c) SAED patterns, (d–e) HR-TEM images, and (f) bright field image and elemental mapping images of CoFe-LDH@NiSe nanosheets detached from NF.

3.2. Structural and compositional characterization of NiSe and CoFe-LDH@NiSe

The heterojunction formation of CoFe-LDH@NiSe was described in detail by XRD studies. In Fig. 3a, the peaks located at 44.5° , 51.9° , and 76.1° correspond to the (111), (200), and (220) planes, respectively, of NF (PDF no. 01-070-1849). As illustrated in the fabrication process (Scheme 1), the first step is the formation of Ni(OH)_2 , in which the XRD pattern shows the diffraction planes (001), (100), (101), (102), (110), and (111) of $\beta\text{-Ni(OH)}_2$ (PDF no. 14-0117) which agrees well with a previous report [62]. After selenization, the peaks of Ni(OH)_2 completely disappeared and transformed into hexagonal NiSe with no additional peaks. This indicates that nickel hydroxide was successfully converted to a NiSe structure upon selenide processing. The highly crystalline peaks of (100), (101), (211), (102), (110), (103), (201), and (202) planes belong to hexagonal NiSe (*h*-NiSe) with lattice parameter ($a = b = 3.66 \text{ \AA}$, $c = 5.33 \text{ \AA}$) (PDF no. 02-0892) [63,64]. The electro-deposited CoFe-LDH material on the NF show the peaks on (003), (006), (012), (015), (110), and (113) planes (PDF no. 082-8040). Finally, the heterostructure of CoFe-LDH@NiSe shows both the hierarchical peaks of the NiSe and CoFe-LDH individual components.

The chemical valence states of the as-prepared NiSe, CoFe-LDH, and CoFe-LDH@NiSe were evaluated using XPS analysis. The individual deconvoluted XPS spectra, as shown in Fig. 3b–f, reveal the existence of surface composition and the corresponding oxidation states of the elements for investigating the synergistic effect of the heterostructure. The high-resolution Ni 2p spectra for NiSe and CoFe-LDH@NiSe shows one spin-orbit doublet peaks at 872.9 ± 0.1 and 854.1 ± 0.1 eV corresponding to $\text{Ni } 2p_{1/2}$ and $\text{Ni } 2p_{3/2}$, respectively (Fig. 3b). These two peaks indicate the presence of the Ni^{2+} oxidation state [65]. The peaks at 878.8 and 860.27 eV are ascribed to satellite structures associated with the formed $\gamma\text{-NiOOH}$, which might be useful

to enhance OER performance. The Se 3d spectra was deconvoluted, the two peaks at $54.9 \text{ eV} \pm 0.1$ and $56.5 \pm 0.1 \text{ eV}$ were attributed to $\text{Se } 3d_{5/2}$ and $\text{Se } 3d_{3/2}$ of Se^{2-} (Fig. 3c). The broad peak at 58.5 eV was attributed to the oxidized selenium species (SeO_x) due to surface oxidation caused by air contact for NiSe. The Se-O bonding peak is slightly shifted to a higher binding energy (58.9 eV), which confirms the bonding with the oxygen moieties of the double hydroxide layer. The above band characteristics agree with previous reports [30,31]. The Co 2p of CoFe-LDH and CoFe-LDH@NiSe deconvoluted core-level spectra show the binding energies of Co $2p_{1/2}$ and Co $2p_{3/2}$ at 796.7 and, 780.8 eV, respectively (Fig. 3d), which are related to the high-spin Co^{2+} state for both CoFe-LDH and CoFe-LDH@NiSe [32]. The Fe 2p deconvoluted high-resolution spectra of CoFe-LDH and CoFe-LDH@NiSe show two spin-orbit peaks located at 724.6 and 711.3 eV (Fig. 3e), which are ascribed to the Fe $2p_{3/2}$ and Fe $2p_{1/2}$ of Fe^{2+} [66]. Compared to CoFe-LDH, the binding energies of Fe $2p_{3/2}$ and Fe $2p_{1/2}$ of CoFe-LDH@NiSe show an obvious shift to lower binding energy of 0.6 and 0.9 eV respectively. These shifts suggest the presence of strong interfacial electronic interactions between NiSe and CoFe-LDH [33]. The peak at 717.1 and 716.5 eV are the satellite peaks of Fe^{2+} ions. The O 1s spectra reveals the presence of three types of bonding that exists in the layer double hydroxide at the binding energies of 530.4 eV, 531.0 eV, and 532.12 eV corresponding to M-O, M-OH, and H_2O of CoFe-LDH respectively (Fig. 3f). CoFe-LDH@NiSe had a slight positive shift of 0.3 eV at binding energies of 530.7 eV, 531.6 eV, and 532.6 eV, demonstrating the typical bonding characteristics of pure CoFe-LDH [67]. From this detailed structural analysis, it can be confirmed that CoFe-LDH@NiSe was successfully fabricated. The OER and the HER performances of CoFe-LDH@NiSe depended on the electron transfer process between Ni, Co, and Fe. The co-existence of these three 3d elements should have an electronic interplay at the interface because of the electronic configurations $\text{Ni}^{2+} [\text{Ar}] 3d^8 (t_2g^6$

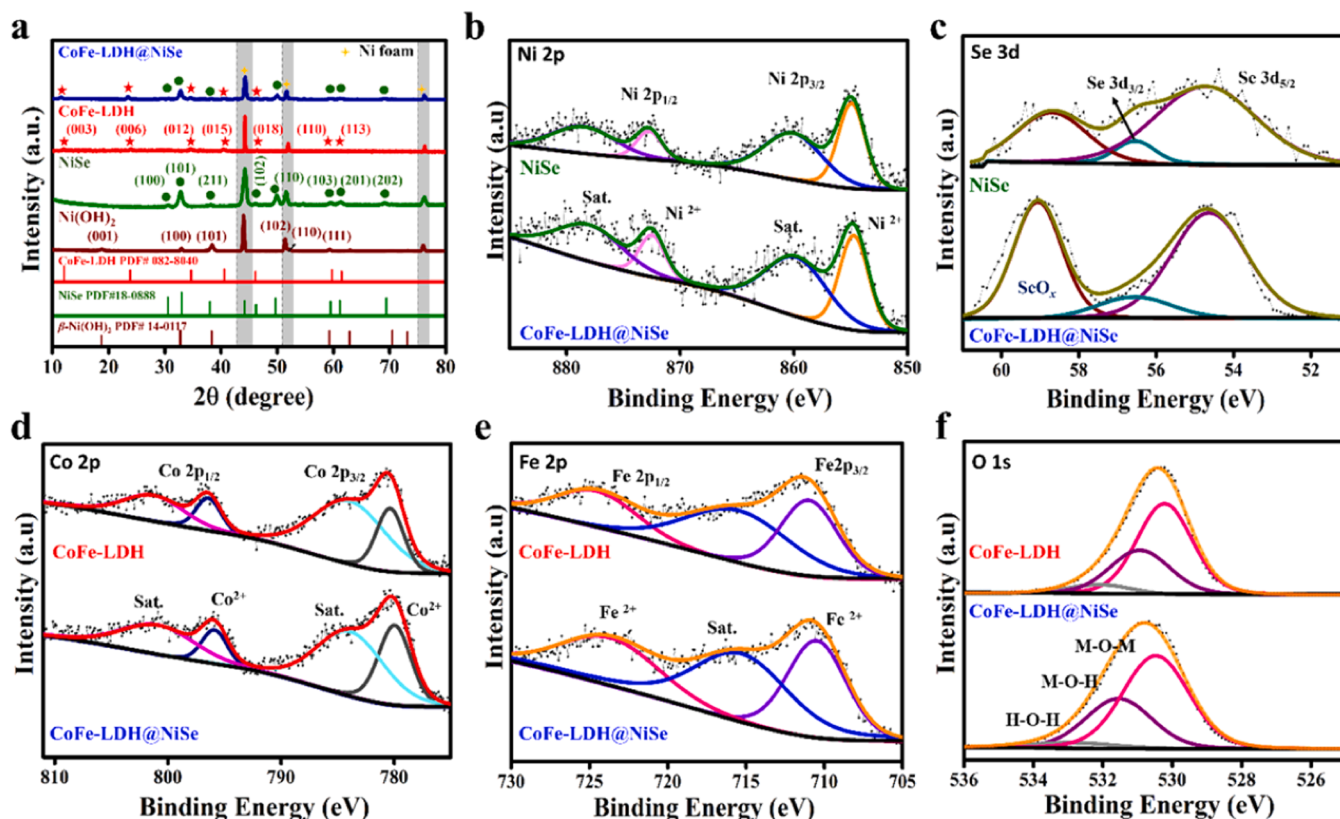


Fig. 3. (a) XRD patterns of Ni(OH)_2 , NiSe, CoFe-LDH, and CoFe-LDH@NiSe. High-resolution deconvoluted XPS spectra of (b) Ni 2p, (c) Se 3d, (d) Co 2p, (e) Fe 2p, and (f) O 1s for NiSe, CoFe-LDH compared with CoFe-LDH@NiSe.

e_g^2), $Fe^{2+}[Ar] 3d^6 (t_{2g}^5 e_g^1)$, and $Co^{2+}[Ar] 3d^7 (t_{2g}^6 e_g^1)$, which undergo oxidation through the loss of an electron via the charge-transfer process, leading to the adsorption of hydroxyl groups in an alkaline medium. Therefore, Ni^{2+} , Co^{2+} , and Fe^{2+} maintain a high valence state (Ni^{3+} , Co^{3+} and Fe^{3+}) in the reaction process for the regeneration of active sites. In contrast, Ni bonded to Se due to electron charge transfer and the formation of NiSe-OOH and Co-O-Fe-O-Ni-O-Co on the surface possessing high reactive species in enhancing OER activity. Furthermore, Raman studies prove the heterostructure formation of CoFe-LDH@NiSe in Fig. S5. Raman spectrum of NiSe shows the small

bands at 181 and 506 cm^{-1} corresponds to Se-Se (A_g-T_g) mode of vibration and longitudinal optical (LO) one phonon mode of NiSe, respectively [68]. In CoFe-LDH, the sharp peaks at 460, 530 and 710 cm^{-1} are associated with Co-O-Co, Co-O-Fe and Fe-O-H vibrations, respectively [69,70]. In CoFe-LDH@NiSe, the peak broadening at 462 and 515 cm^{-1} corresponds to Ni/Co-O-Co and Ni/Co-O-Fe vibration, respectively. The raise in peak intensity at 640 cm^{-1} corresponds to Ni-O, Co-O stretching vibration and the peak at 710 cm^{-1} related to Fe-O-H vibration [71]. From the Raman results it can be identified that Ni-O-Co or Ni-O-Fe bonds were coexist in CoFe-LDH@NiSe

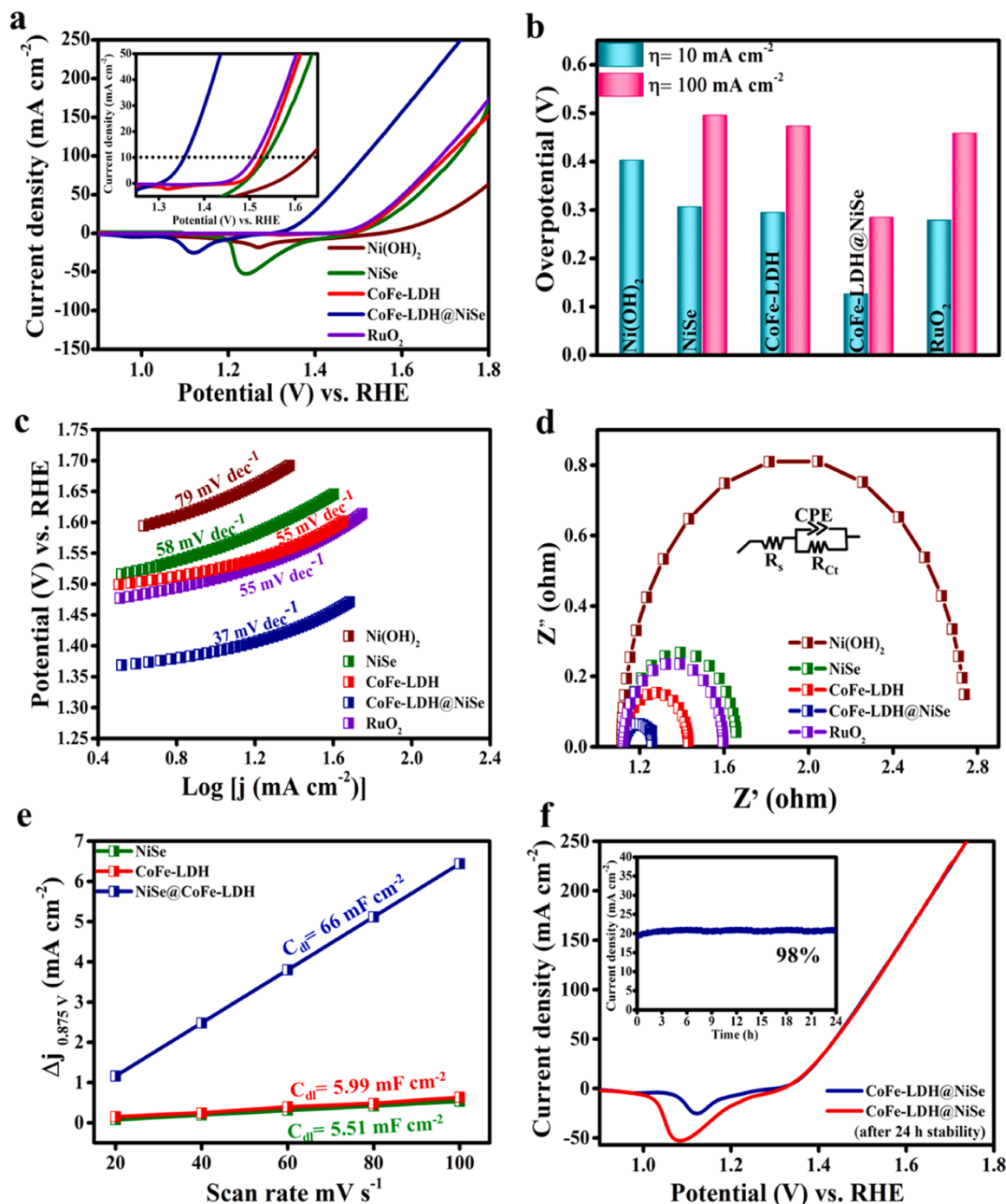


Fig. 4. OER performance of commercial RuO_2 , $Ni(OH)_2$, NiSe, CoFe-LDH, and CoFe-LDH@NiSe catalysts: (a) LSV curves, (b) comparison of the overpotential at current densities of 10 and 100 mA cm^{-2} , (c) Tafel plots derived from steady-state polarization curves in 1.0 M KOH for OER, (d) Nyquist plots corresponding to (c), (e) capacitive Δj ($\Delta j = j_a - j_c$) vs scan rates of NiSe, CoFe-LDH, and CoFe-LDH@NiSe, (f) durability test of CoFe-LDH@NiSe before and after 24 h cycles; inset chronoamperometry tests of CoFe-LDH@NiSe at a current density of 20 mA cm^{-2} .

heterostructure. The interfacial coupling of CoFe—LDH@NiSe water oxidation and reduction levels is beneficial for the overall water splitting process [72].

3.3. Electrocatalytic oxygen evolution reaction of CoFe—LDH@NiSe

The OER performance of CoFe—LDH@NiSe was evaluated in a 1.0 M KOH electrolytic solution using a three-electrode system. First, LSV curves were evaluated for Ni(OH)₂, NiSe, CoFe—LDH, CoFe—LDH@NiSe, and commercial RuO₂ at a scan rate of 2 mV s⁻¹ (Fig. 4a). Herein, the LSV measurements were carried out in a negative scan due to the strong redox peak persisted in the positive scan [32]. The strong redox behavior in NiSe, CoFe—LDH, and CoFe—LDH@NiSe can be clearly observed from the full CV curves shown in Fig. S6, where less overpotential is observed than the actual range in forward scan. To calculate accurate overpotential LSV was performed from higher to lower potential range. CoFe—LDH@NiSe delivered the lowest overpotential of 127 mV at 10 mA cm⁻², which was significantly lower than that of the individual counterpart catalyst of Ni(OH)₂ (403 mV), NiSe (307 mV), CoFe—LDH (295 mV), and state-of-the-art RuO₂ (279 mV). Notably, CoFe—LDH@NiSe required only an overpotential 285 mV to deliver a higher current density of 100 mA cm⁻² which is comparatively lower than the water oxidation efficiency of CoNi-, NiFe-, CoFe- and ZnCo-LDH ultrathin nanosheets overpotential 320, 290, 285, and 345 mV at 10 mA cm⁻² [73]. In contrast, NiSe, CoFe—LDH, and RuO₂ required high overpotentials of 496 mV, 474 mV, 367 mV, and 459 mV at a current density of 100 mA cm⁻². A detailed overpotential histogram is shown in Fig. 4b. The outstanding OER performance of CoFe—LDH@NiSe also surpasses other transition metal heterostructure catalysts of CoSe/NiFe—LDH (η_{10} = 201 mV) [32], CoFe@NiFe—LDHs (η_{10} = 190 mV) [33], Co₃O₄@NiFe—LDH (η_{100} = 276 mV) [41], NiSe@NiFe—LDH (η_{100} = 240 mV) [42], ultrathin NiFe—LDH nanosheets (η_{100} = 286 mV) [43], and NiFe—LDH@NiCoP (η_{100} = 210 mV) [44] at 10 mA cm⁻² and 100 mA cm⁻² in alkaline medium supported on NF, as shown in Table S1. The Tafel slope was used to verify the kinetic activity of the catalyst using the equation $\eta = a + b \log(j)$, where η , a , b , and j represent the overpotential, constant, Tafel slope, and current density, respectively.

As expected, CoFe—LDH@NiSe had a significantly lower Tafel slope of 37 mV dec⁻¹ compared to commercial RuO₂ (55 mV dec⁻¹), individual CoFe—LDH (55 mV dec⁻¹), NiSe (58 mV dec⁻¹), and Ni(OH)₂ (78 mV dec⁻¹) (Fig. 4c). In addition, the Tafel values obtained for CoFe—LDH and NiSe exhibited Tafel slopes similar to that of commercial RuO₂. The reduction in the Tafel slope resulted from the heterojunction interface engineering of both materials, where the catalytic activity of CoFe—LDH@NiSe increased considerably compared to other heterostructure materials listed in Table S1. To investigate the OER kinetics of the catalysts, the EIS profiles of CoFe—LDH@NiSe and the as-prepared individual electrocatalysts were also determined in 1.0 M KOH. Fig. 4d shows the corresponding Nyquist plots, which can be clearly note that the charge-transfer resistance (R_{ct}) of CoFe—LDH@NiSe (1.25 Ω) is much smaller than that of CoFe—LDH (1.42 Ω), commercial RuO₂ (1.59 Ω), NiSe (1.66 Ω), and Ni(OH)₂ (2.74 Ω). Consequently, CoFe—LDH@NiSe exhibited the fastest charge-transfer rate and the most facile catalytic kinetics toward the OER among all the samples. The enhanced catalytic kinetics of CoFe—LDH@NiSe is attributed to the close integration and strong electronic interactions between the NiSe and CoFe—LDH nanosheets. The electrochemical active areas (ECSA) of the NiSe, CoFe—LDH, and CoFe—LDH@NiSe catalysts were also estimated according to the double-layer capacitance (C_{dl}) determined via CV in the non-faradaic region at different scan rates of 20, 40, 60, 80, and 100 mV s⁻¹ (Fig. S7). In the slope of the capacitive current ($j_{anode} - j_{cathode}$) plots at 0.875 V (vs. RHE) versus scan rates, the CoFe—LDH@NiSe catalyst possessed a larger C_{dl} of 66 mF cm⁻², which is higher than that of CoFe—LDH (5.99 mF cm⁻²), and significantly higher than that of NiSe (5.51 mF cm⁻²) (Fig. 4e). This implies much

higher ECSA and augmented active sites via the interfacial coupling of NiSe and CoFe—LDH. For large-scale applications, the durability of the CoFe—LDH@NiSe catalyst was also tested using a chronoamperometry method at a current density of 20 mA cm⁻² (Fig. 4f), which maintained 98% retention for more than 24 h. Simultaneously, the LSV curves of the CoFe—LDH@NiSe catalysts before and after 24 h were nearly unchanged with robust stability. The increment in the growth of cathodic peak even after 24 h stability is due to the influence of nickel [74]. Additionally, the chronopotentiometry tests were performed at 50 mA cm⁻² for 24 h, which deliver the superior stability at 1.456 V (Fig. S8). Further the stability of the catalyst after OER test was characterized using XRD, SEM and TEM, as shown in Fig. S9. It can be observed from images that the CoFe—LDH@NiSe structure exhibits excellent durability and stability after 24 h.

The superior OER activity of CoFe—LDH@NiSe is explained by the following: 1) the prepared heteronanostructures via interfacial coupling are beneficial for enhancing the OER properties, which offer a larger specific surface area. The morphology of nanosheets with defects provides more active sites for promoting the rapid diffusion of the electrolyte into the catalyst on the surface, thereby ensuring good electron transport; 2) the coordination of three 3d transition elements Fe, Co, and Ni easily lose their electrons due to the ease of variable oxidation states. Consequently, the release of electrons favors the charge-transfer process. The electron release phenomenon governed by the electronegativity factor proposed by Paul's principle supports the oxygen scavenging property; 3) the presence of interface engineering between these elements creates an electron-rich domain from Fe to Co to Ni, which enables partial transfer phenomena and makes electron-rich regeneration active sites throughout the OER process [75]. Additionally, CV curves at various scan rates of 2, 5, 10 and 20 mV s⁻¹ demonstrate the electron transfer process in CoFe—LDH@NiSe via redox processes at 1.1–1.4 V (Fig. S10). It should be noticed that with the increasing scan rate the potential of the cathodic and anodic peaks shifts to more negative and positive directions, respectively. We note that the redox peak shifts negatively due to the synergetic effect from between Ni and Co, which was reported to increase the activity and reversibility of Ni²⁺/Ni³⁺ [76]. This can also be inferred from the XPS spectra after the OER process (Fig. S11). The possible reaction mechanism based on the Krasil'shchikov pathway process is that Ni²⁺ [Ar] 3d⁸ ($t_{2g}^6 e_g^2$) may undergo oxidation and attain the higher oxidation state of Ni³⁺ ($t_{2g}^6 e_g^1$) by the loss of an electron and sharing of the electron with Se²⁻. Similarly, Fe²⁺ [Ar] 3d⁶ ($t_{2g}^5 e_g^1$) and Co²⁺ [Ar] 3d⁷ ($t_{2g}^6 e_g^1$) reached a higher oxidation state of Fe³⁺ [Ar] 3d⁵ ($t_{2g}^4 e_g^1$) and Co³⁺ ($t_{2g}^5 e_g^1$). The donation of electrons from Fe, Co to Ni maintains a rich electron domain in all these species and makes the OER process efficient. The release of electrons and the generation of active sites adsorb the water hydroxyl ions (OH⁻) to form oxy-hydroxides of Ni—OOH, NiSe—OOH, Co—OOH, and Fe—OOH on the catalytic surface. This is supported by the O 1s spectra, where the contribution from M—O increased significantly compared to that of the as-synthesized catalyst [25,39,42,67]. Subsequently, oxygen molecules are released during the reduction process.

3.4. DFT results of potential dependent free energies

To further elucidate the underlying mechanism of the improved OER on CoFe—LDH@NiSe, we performed site analysis of NiSe (110) and 2D CoFe—LDH to determine the active sites for the OER. The simulated surfaces (top and side views) of NiSe, CoFe—LDH, and CoFe—LDH@NiSe are shown in Fig. 5a, and the details of the simulated systems are shown in the Supporting Information (Fig. S12). Prior to investigating the potential dependent free energy, site analysis was performed on NiSe (110) and CoFe—LDH to determine the active sites for the OER. On the NiSe (110) surface, there are two potential active sites for Ni and Se. DFT simulations evaluating the stability of OER intermediates (OH*, O*, and OOH*) show that the intermediates (OH* and OOH*) on the Ni site are more energetically stable than the Se site (Fig. S13). In terms of

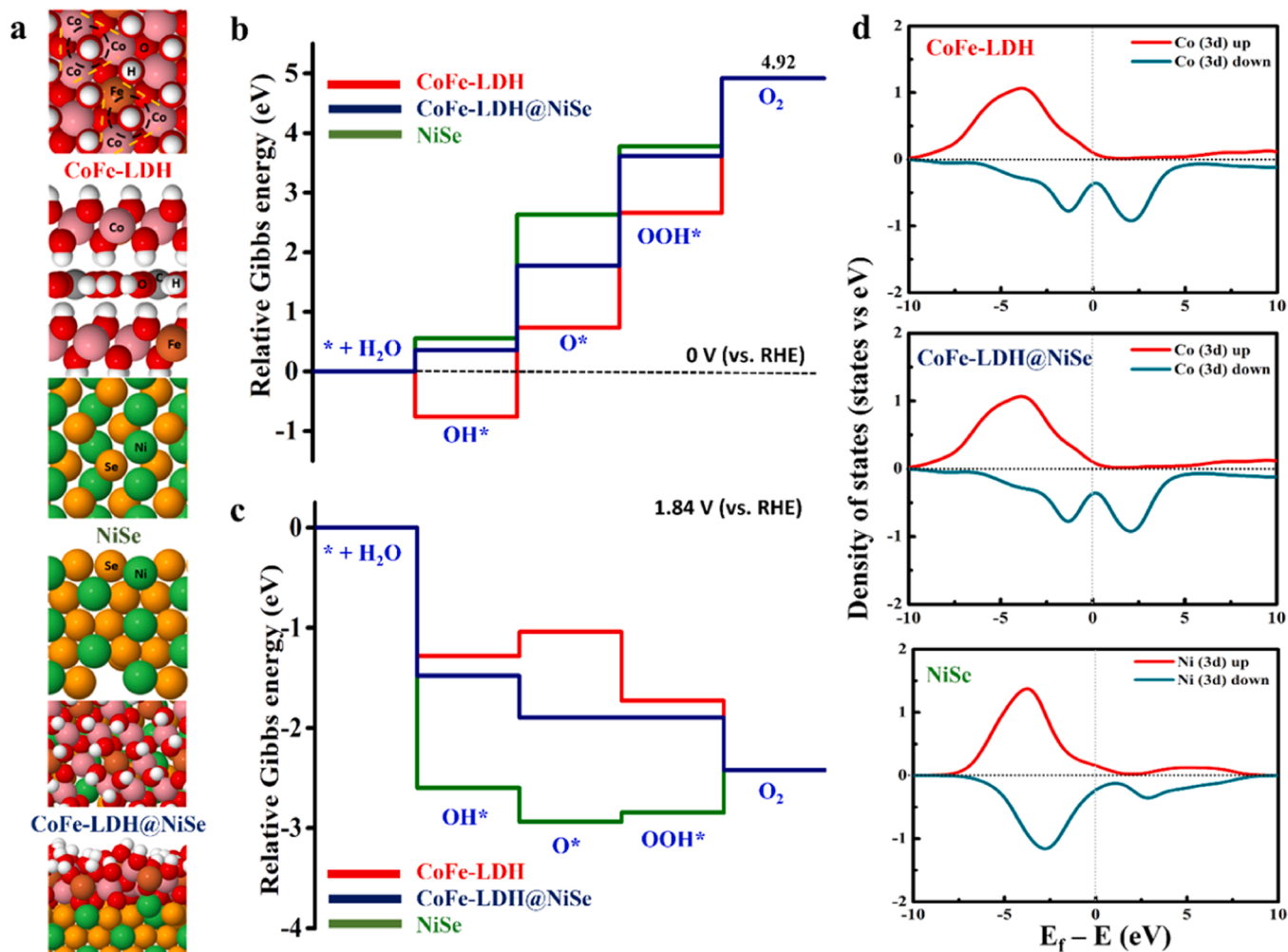


Fig. 5. (a) DFT relaxed configurations of CoFe-LDH, NiSe, CoFe-LDH@NiSe surfaces; (b and c) DFT evaluated free energy diagrams for OER on NiSe, CoFe-LDH and CoFe-LDH@NiSe surfaces at 0 V and 1.84 V (vs. RHE) with 13 H surface hydrogen concentration at Co—Co—Co active site; (d) Partial density of states of 3d orbitals for Ni of NiSe, Co of CoFe-LDH and Co of CoFe-LDH@NiSe with respect to the Fermi level (E_f). The vertical dotted line represents E_f at 0 eV.

CoFe-LDH, the OER intermediates on the surface can adsorb at two different hollow sites, Co—Co—Co and Co—Fe—Co (Fig. 5a). These sites are indicated by the yellow-dashed triangles. DFT simulation evaluating the potential dependent free energies of the OER mechanism predicts that both sites of Co—Co—Co and Co—Fe—Co on CoFe-LDH provide similar OER performance (Fig. S15). In contrast to the CoFe-LDH results, the CoFe-LDH@NiSe surface shows better OER performance on Co—Co—Co sites than on Co—Fe—Co sites. Hence, we focused on the Co sites for CoFe-LDH and CoFe-LDH@NiSe, and Ni sites for NiSe (110). More details of the site analysis and potential dependent free energies with different active sites are shown in Fig. S14.

Fig. 5b shows the DFT-predicted ΔG (OER) diagrams with respect to the three surfaces at 0 V (vs. RHE). CoFe-LDH showed the most stable OER intermediates (OH*, O*, OOH*), followed by CoFe-LDH@NiSe and NiSe. However, CoFe-LDH has a potential determining step at the end (OOH* \rightarrow O₂). This large energy gap requires a high onset potential to spontaneously proceed with the OER on the CoFe-LDH. In contrast, the higher ΔG (nonspontaneous) of OER intermediates on NiSe (110) and CoFe-LDH@NiSe surfaces led to lower onset potentials for the last step toward O₂ evolution. Fig. 5c shows the OER ΔG diagrams at the onset potential of 1.84 V (vs. RHE) for NiSe, CoFe-LDH, and CoFe-LDH@NiSe. The NiSe and CoFe-LDH provide nonspontaneous steps of the O* (NiSe), OOH* (CoFe-LDH), and O₂ (CoFe-LDH) steps at 1.84 V. Similar observations have been reported in the literature [77, 78]. As mentioned above, the OER results at the Co—Fe—Co site provide

similar trends of OER on Co—Co—Co sites, but Co—Fe—Co sites are less active than Co—Co—Co sites which is further explained in Fig. S18. The comparison results imply that the experimentally observed high OER reactivity of CoFe-LDH@NiSe is attributed to the Co—Co—Co active site. Overall, the DFT predictions for OER performance agree well with our experimental results that NiSe-supported CoFe-LDH shows better OER performance than the other systems at similar applied potentials. Electronic structure analysis was conducted to elucidate the origins of the different reactivities. Fig. 5d presents the partial density of states (pDOS) of the *d* orbitals (Ni and Co) on the NiSe, CoFe-LDH, and CoFe-LDH@NiSe surfaces. The significant differences between the *d* orbitals of the NiSe, CoFe-LDH, and CoFe-LDH@NiSe systems were observed. The CoFe-LDH systems have more unoccupied states near the Fermi level compared to those of NiSe. The more unoccupied states trigger strong donation interactions from the HOMO of intermediates to the unoccupied *d*-band, thereby stabilizing the adsorbed molecules [79]. The more stabilized OER intermediates correspond to more spontaneous steps during the OER (except for the last step of O₂ desorption). Therefore, it is expected that the higher OER performance of CoFe-LDH systems is driven by strong donation interactions due to the presence of an unoccupied state near the Fermi level. In contrast to the distinguished pDOS between NiSe and CoFe-LDH systems, a considerable difference was not found between CoFe-LDH and CoFe-LDH@NiSe, demonstrating that the *d*-band centers of both surfaces were almost identical (CoFe-LDH: -3.64 eV and CoFe-LDH@NiSe: -3.61 eV). These

indistinguishable results suggest that both surfaces undergo similar covalent interactions between the *d* orbitals and molecular orbitals of the OER intermediates [80–82]. Since we did not find any evidence of covalent interactions, we focused on the ionic interactions strongly triggered by the difference in work functions ($\Delta W = W - W_0$) between the system and OER intermediate (O^*) [82]. The work function of the system is evaluated by $W = E_v - E_f$, where E_v and E_f are the vacuum energy and Fermi level, respectively. The work function of the adsorbate can be regarded as the HOMO of the adsorbate because $E_f - E_v$ of the molecule is the same as that of the HOMO. The ionic interactions have been suggested to be proportional to the ΔW^2 meaning that a larger gap between

the work functions provides stronger ionic interactions [82]. Finally, we evaluated the ΔW^2 of CoFe–LDH and CoFe–LDH@NiSe which showed that CoFe–LDH has a larger ΔW^2 (8.62) than CoFe–LDH@NiSe (1.68). These significant differences in ΔW^2 generate different stabilities of OER intermediates, which provide different OER performances with identical densities of states. The larger ΔW^2 of CoFe–LDH reflects strong spontaneous OER steps, but the ionic interactions are too strong to cause intermediates to desorb from the surface (large nonspontaneous step of $OOH^* \rightarrow O_2(g) + * + \frac{1}{2}H_2(g)$). However, because CoFe–LDH@NiSe has a smaller ΔW^2 , it is sufficient to make the OER steps spontaneous that do not trigger strong interactions for the O_2 desorption step. It should be

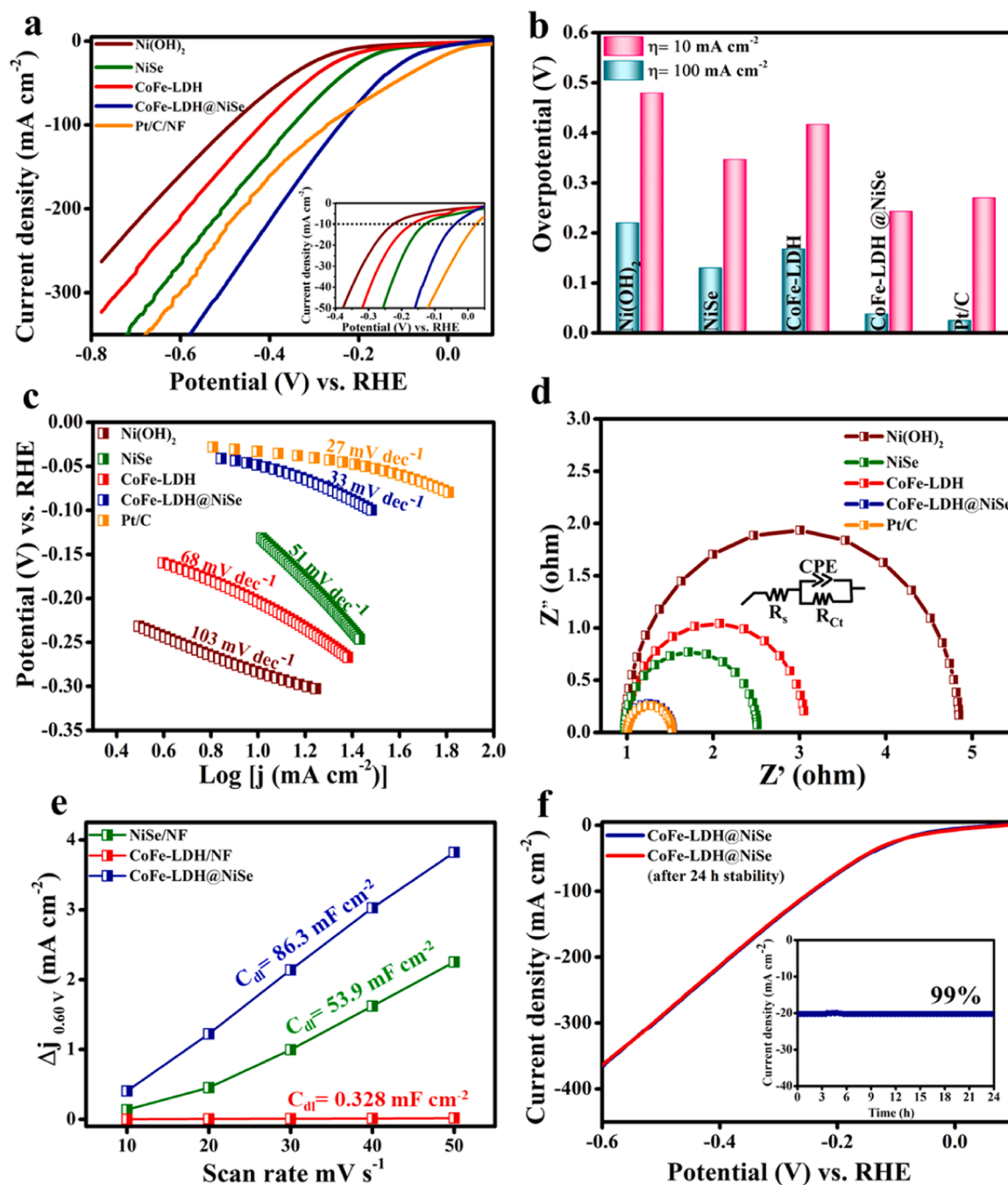


Fig. 6. HER performance of Pt/C, $Ni(OH)_2$, $NiSe$, $CoFe-LDH$, $CoFe-LDH@NiSe$ catalysts; (a) LSV curves, (b) comparison of the overpotential at current densities of 10 and $100\ mA\ cm^{-2}$, (c) Tafel plots derived from steady-state polarization curves for OER, (d) Nyquist plots corresponding to (c), (e) capacitive Δj ($\Delta j = j_a - j_c$) vs scan rate of as-prepared samples and the corresponding linear slopes, (f) LSV curves before and after 24 h durability test and inset chronoamperometry tests of $CoFe-LDH@NiSe$ at a current density of $20\ mA\ cm^{-2}$.

noted that CoFe–LDH@NiSe has a similar d-band of CoFe–LDH, strengthening the covalent interactions and has a similar vacuum energy of NiSe (NiSe = 3.56 eV, CoFe–LDH@NiSe = 3.10 eV and CoFe–LDH = 0.95 eV), which affects the work function, resulting in the weakening of the ionic interactions. Therefore, it can be concluded that the compromised effects make the free energy profiles of CoFe–LDH@NiSe remain in the middle of NiSe and CoFe–LDH, thereby enhancing the overall OER reactivity. We believe that a more detailed analysis based on the electronic structure to understand different OER reactivity is needed; however, such an analysis is beyond the scope of this paper. We will perform a more in-depth study to obtain more insights into the different reactivities of the heterostructure in our future study.

3.5. Electrocatalytic hydrogen evolution reaction of CoFe–LDH@NiSe

Inspired by the OER performance of the as-prepared electrocatalyst, the HER performance of Ni(OH)₂, NiSe, CoFe–LDH, and CoFe–LDH@NiSe was further investigated in a 1.0 M KOH solution in comparison with the commercial 20 wt% Pt/C coated on NF. The LSV profile of CoFe–LDH@NiSe demonstrates the excellent electrocatalytic performance toward HER, achieving a cathodic current density of 10 mA cm^{−2} at a very low overpotential of 38 mV, which is merely equal to that of Pt/C (2.5 mV) and significantly lower than those of NiSe (126 mV), CoFe–LDH (169 mV), and Ni(OH)₂ (224 mV) (Fig. 6a). In addition, CoFe–LDH@NiSe delivered a significantly lower overpotential of 238 mV at a current density of −100 mA cm^{−2} compared to that of Pt/C (270 mV). The detailed overpotential histograms at current densities of −10 and −100 mA cm^{−2} for all samples are shown in Fig. 6b. The HER performances of CoFe–LDH@NiSe is superior to that of CoSe@NiFe–LDH (η_{10} = 98 mV) [32], Hierarchical values of CoFe@NiFe–LDHs (η_{10} = 240 mV) [33], Co₃O₄@NiFe–LDH (η_{10} = 74 mV) [41], NiSe@NiFe–LDH (η_{100} = 276 mV) [42], ultrathin NiFe–LDH nanosheets (η_{100} = 222 mV) [43] are listed in Table S1. The HER kinetic reactions of the as-prepared electrocatalysts were further examined using Tafel plots (Fig. 6c), which were derived from the corresponding LSV curves. The Tafel value of CoFe–LDH@NiSe (33 mV dec^{−1}) is closer to that of Pt/C (27 mV dec^{−1}) and lower than those of NiSe (51 mV dec^{−1}), CoFe–LDH (68 mV dec^{−1}), and Ni(OH)₂ (103 mV dec^{−1}), demonstrating that the CoFe–LDH@NiSe catalyst has excellent reaction kinetics and abundant active sites for HER performance. The extraordinary performance of CoFe–LDH@NiSe can be explained using the “Volmer–Heyrovsky” mechanism or Tafel process, which is considered to be the rate-determining step for the HER. Based on the Volmer mechanism, the d electrons in Ni (Ni²⁺–t_{2g}⁶ e_g² and Ni³⁺–t_{2g}⁶ e_g¹), Co (Co²⁺–t_{2g}⁶ e_g¹, Co³⁺–t_{2g}⁵ e_g¹), Fe²⁺ [Ar] 3d⁶ (t_{2g}⁵ e_g¹), and Fe³⁺ [Ar] 3d⁵ (t_{2g}⁴ e_g¹) can be easily removed. Therefore, the first step is the dissociation of H₂O adsorbed on the surface via an easier electron transfer process with e_g almost equal to unity, which results in the formation of H* radicals and OH[−] (generated by the Volmer mechanism). The second step is the combination of this H* radical with another H* radical via the deprotonation process, followed by H₂ release (Tafel process). As discussed above, Ni²⁺/Ni³⁺, Co²⁺/Co³⁺, and Fe²⁺/Fe³⁺ are considered as the active centers, and Se^{2−} is coordinated via hydrogen bonding. High conductivity, thereby enhancing the durability and catalytic activity for the HER performance, aids in this reaction. However, the individual electrocatalyst NiSe is more active than CoFe–LDH with the support of Se^{2−}, where the conductivity is increased. Therefore, the electrons of Ni (Ni²⁺–t_{2g}⁶ e_g² and Ni³⁺–t_{2g}⁶ e_g¹) share Se^{2−} and maintain their valence states. However, Co (Co²⁺–t_{2g}⁶ e_g¹ and Co³⁺–t_{2g}⁵ e_g¹) with Fe²⁺ [Ar] 3d⁶ (t_{2g}⁵ e_g¹) and Fe³⁺ [Ar] 3d⁵ (t_{2g}⁴ e_g¹) for CoFe–LDH sharing of electron pairs limit the process where higher energy is required for the imitiation step. Fig. 6d presents Nyquist plots with an equivalent circuit used to fit the spectra. The R_{ct} of Pt/C and CoFe–LDH@NiSe is approximately 1.52 Ω with a smaller semicircle, indicating fast electron transfer and lower charge-transfer resistance, leading to enhance HER performance. The individual samples have a

significantly higher R_{ct} for NiSe (2.55 Ω), CoFe–LDH (3.03 Ω), and Ni(OH)₂ (4.86 Ω), which agreed with those of Tafel and LSV. The ECSA of the catalysts was also estimated from the CV curves at different rates of 10–50 mV s^{−1} (Fig. S19). From the slope of the capacitive current ($j_{\text{anode}} - j_{\text{cathode}}$) plots at 0.60 V (vs. RHE) versus scan rates, the CoFe–LDH@NiSe catalyst possessed a higher C_{dl} of 0.88 mF cm^{−2}, which is higher than that of NiSe (0.55 mF cm^{−2}), and significantly higher than that of CoFe–LDH (0.32 mF cm^{−2}) (Fig. 6e). The durability of the CoFe–LDH@NiSe catalyst is essential for determining its HER performance for industrial applications.

Hence, CV and chronoamperometry (CA) studies were carried out for CoFe–LDH@NiSe for long-term analysis. Fig. 6f shows the LSV curves of CoFe–LDH@NiSe before and after 24 h of CA stability, demonstrating its remarkable stability. The inset in Fig. 6f shows the chronoamperometry results, producing a stable current density of −20 mA cm^{−2} for 24 h with 99% retention. Furthermore, the chronopotentiometry tests were performed at −50 mA cm^{−2} for 24 h, which achieved the remarkable stability for HER at −0.156 V (Fig. S20). The stability of the CoFe–LDH@NiSe was characterized using XRD, SEM and TEM (Fig. S21). It can be observed from images that the CoFe–LDH@NiSe structure exhibits excellent durability and stability after 24 h. With the outstanding high efficiency and stability of the as-prepared electrocatalysts for both OER and HER, a two-electrode cell of CoFe–LDH@NiSe was assembled as the anode and cathode for overall water splitting in 1.0 M KOH. For comparison, NiSe and CoFe–LDH were also tested, and the LSV curves are shown in Fig. 7a. The CoFe–LDH@NiSe required 1.51 V to deliver 10 mA cm^{−2} current density which is significantly lower than CoFe–LDH (1.63 V) and NiSe (1.70 V). A digital image of the bifunctional nature of CoFe–LDH@NiSe on alkaline water splitting is shown in Fig. 7b. The long-term stability test for 120 h (5 days) suggests unchanged activity at 1.51 V of ~10 mA cm^{−2}, with an impressive 98% activity retention. Strikingly, the stability of CoFe–LDH@NiSe was also performed in harsh condition to identify the robustness of catalyst (Fig. S22). The CoFe–LDH@NiSe required 1.99 V to deliver 100 mA cm^{−2} (harsh current density), which is significantly lower than CoFe–LDH (2.03 V) and NiSe (2.08 V). Moreover, the stability test of CoFe–LDH@NiSe for 24 h suggests unchanged activity at 1.99 V with 100 mA cm^{−2}. A digital image of the bifunctional nature of CoFe–LDH@NiSe on alkaline water splitting is shown in the inset Fig. S22.

The outstanding ability of CoFe–LDH@NiSe for overall water splitting is confirmed by comparing its activity (1.51 V for 10 mA cm^{−2}) with the recently reported NF-based materials such as CoSe/NiFe–LDH (1.53 V) [32], Hierarchical CoFe@NiFe–LDHs (1.57 V) [33], Co₃O₄@NiFe–LDH (1.56 mV) [41], NiSe@NiFe–LDH (1.53 V) [42], ultrathin NiFe–LDH nanosheets decorated on V-doped Ni₃S₂ nanorod arrays (1.55 V) [43], NiFe–LDH@NiCoP electrodes (1.54 V) [44], Co₉S₈@Ni₃S₂ heterointerfaced nanotubes (1.59 V) [83], 3D hierarchical nanoarchitecture Cu@NiFe–LDH (1.54 V) [84], 3D hierarchical nanoarchitecture Cu@CoFe–LDH (1.68 V) [85], FeS₂ (1.67 V) [86], Ni_{0.3}Co_{0.7}-9AC-AD/NF (1.56 V) [87], NiVB@rGO (1.46 V) [88] and 2D Co₂P@Co₃O₄ (1.57 V) [89] are summarized in Table S1. In addition, chronoamperometry tests were carried out to verify the performance of CoFe–LDH@NiSe for 24 h at a current density of 10 mA cm^{−2} at 1.51 V (Fig. 7c).

The overall results suggest that the outstanding OER and HER performance of CoFe–LDH@NiSe can be attributed to the following aspects. First, the strong interfacial coupling enhances the electronic interaction and the synergistic effect on the interface of the NiSe and CoFe–LDH heterostructure, which could facilitate the electron transfer process. Second, the defects and vacant oxygen vacancies proposed by DFT simulations contribute to the enhancement of the intrinsic OER and HER catalytic activity. Furthermore, the exceptional stability of the CoFe–LDH@NiSe electrocatalyst can be attributed to the template-free design and strongly connected behaviors between the layers between the two catalysts, which is an important factor in water splitting.

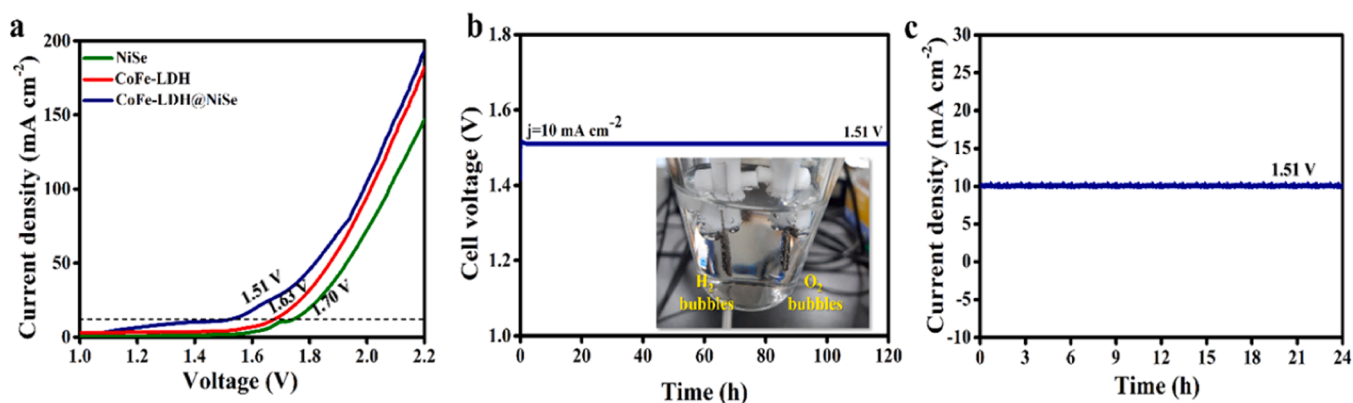


Fig. 7. (a) LSV curves of water electrolysis for as-prepared electrocatalysts in a two-electrode cell with a scan rate of 5 mV s^{-1} in 1.0 M KOH , (b) chronopotentiometry profiles for water electrolysis for 120 h with digital image of water splitting by CoFe-LDH@NiSe, and (c) chronoamperometry tests of CoFe-LDH@NiSe at the current density of 20 mA cm^{-2} .

Therefore, our work has revealed the enhanced electrocatalytic performance of CoFe-LDH@NiSe, leading to high HER and OER performance with long-lasting electrochemical energy conversion devices.

4. Conclusion

We fabricated a CoFe-LDH@NiSe heteronanostructure on NF using a facile hydrothermal and electrodeposition method to obtain efficient electrocatalysts for the OER and the HER performance. The as-prepared CoFe-LDH@NiSe comprised hierarchical 2D nanosheets that provided additional active sites, enhancing the electrocatalytic activity. CoFe-LDH@NiSe exhibited superior OER and HER performance compared to individual CoFe-LDH and NiSe electrocatalysts in an alkaline medium. The CoFe-LDH@NiSe delivered low overpotentials of 127 mV and 38 mV and low Tafel slope values of 37 mV dec^{-1} and 33 mV dec^{-1} at a current density of 10 mA cm^{-2} . It also delivered an extremely low overpotential of approximately 295 and 235 mV at a current density of $\sim 100 \text{ mA cm}^{-2}$ for the OER and the HER, respectively. Impressively, DFT simulation also confirms our experimental results that the interfacial coupling of heteronanostructures plays a vital role in enhancing the electrochemical performance of the CoFe-LDH@NiSe electrocatalyst. This low-cost synthesis is expected to afford remarkable electrocatalysts for large-scale H_2 production applications. In particular, CoFe-LDH@NiSe required a cell voltage of 1.51 V to deliver a current density of 10 mA cm^{-2} and exhibited robust stability for 5 days, which shows potential for industrial applications. This type of highly conductive electrocatalyst has a wide range of applications in different fields, such as energy storage and conversion systems, fuel cells, and hybrid supercapacitors.

CRediT authorship contribution statement

Shrine Maria Nithya Jeghan: Conceptualization, Methodology, Investigation, Formal analysis, Validation, Data curation, Writing – original draft. **Dongjoon Kim:** Software, Methodology, Investigation, Formal analysis, Validation, Data curation, Writing – original draft. **Yuhyeon Lee:** Investigation, Formal analysis, Data curation. **Minkyu Kim:** Software, Validation, Formal analysis, Supervision, Project administration, Writing – review & editing. **Gibaek Lee:** Conceptualization, Investigation, Data curation, Validation, Formal analysis, Supervision, Project administration, Writing – review & editing.

Declaration of Competing Interest

The authors declare no competing financial interest.

Acknowledgments

This research was supported by the Basic Science Research Program through the National Research Foundation of Korea (NRF) funded by the Ministry of Education (NRF-2019R1I1A3A01046928) and “Human Resources Program in Energy Technology” of the Korea Institute of Energy Technology Evaluation and Planning (KETEP) and granted financial resources from the Ministry of Trade, Industry & Energy, Republic of Korea. (No. 20204010600100).

Appendix A. Supporting information

Supplementary data associated with this article can be found in the online version at [doi:10.1016/j.apcatb.2022.121221](https://doi.org/10.1016/j.apcatb.2022.121221).

References

- [1] P. Zhou, X. Lv, D. Xing, F. Ma, Y. Liu, Z. Wang, P. Wang, Z. Zheng, Y. Dai, B. Huang, High-efficient electrocatalytic overall water splitting over vanadium doped hexagonal $\text{Ni}_{0.2}\text{Mo}_{0.8}\text{N}$, *Appl. Catal. B* 263 (2020), 118330.
- [2] K. Kannimuthu, K. Sangeetha, S.S. Sankar, A. Karmakar, R. Madhu, S. Kundu, Investigation on nanostructured Cu-based electrocatalysts for improvising water splitting: a review, *Inorg. Chem. Front.* 8 (2021) 234–272.
- [3] N.L. Garland, D.C. Papageorgopoulos, J.M. Stanford, Hydrogen and fuel cell technology: progress, challenges, and future directions, *Energy Procedia* 28 (2012) 2–11.
- [4] C.M. Kalamaras, A.M. Efstathiou, Hydrogen production technologies: current state and future developments, *Conf. Pap. Sci.* 2013 (2013), 690627.
- [5] Y. Li, R. Li, D. Wang, H. Xu, F. Meng, D. Dong, J. Jiang, J. Zhang, M. An, P. Yang, A review: target-oriented transition metal phosphide design and synthesis for water splitting, *Int. J. Hydrog. Energy* 46 (2021) 5131–5149.
- [6] B. You, Y. Sun, Innovative strategies for electrocatalytic water splitting, *Acc. Chem. Res.* 51 (2018) 1571–1580.
- [7] X. Shang, J.-H. Tang, B. Dong, Y. Sun, Recent advances of nonprecious and bifunctional electrocatalysts for overall water splitting, *Sustain. Energy. Fuels* 4 (2020) 3211–3228.
- [8] V.S. Kumbhar, L. Hyeonkwon, L. Jaeyoung, L. Kiyoun, Recent advances in water-splitting electrocatalysts based on manganese oxide, *Carbon Resour. Convers.* 2 (2019) 242–255.
- [9] D. Wu, K. Kusada, S. Yoshiaki, T. Yamamoto, T. Toriyama, S. Matsumura, Y. Chen, O. Seo, J. Kim, C. Song, S. Hiroi, O. Sakata, T. Ina, S. Kawaguchi, Y. Kubota, H. Kobayashi, H. Kitagawa, Efficient overall water splitting in acid with anisotropic metal nanosheets, *Nat. Commun.* 12 (2021) 1145.
- [10] Y. Lee, J. Suntivich, K.J. May, E.E. Perry, Y. Shao-Horn, synthesis and activities of rutile IrO_2 and RuO_2 nanoparticles for oxygen evolution in acid and alkaline solutions, *J. Phys. Chem. Lett.* 3 (2012) 399–404.
- [11] M.E.C. Pasquazzi, J.P. Hofmann, E.J.M. Hensen, Promoting oxygen evolution of IrO_2 in acid electrolyte by Mn, *Electrochim. Acta* 366 (2021), 137448.
- [12] H. Yoo, K. Oh, Y. Ri Lee, K.H. Row, G. Lee, J. Choi, Simultaneous co-doping of RuO_2 and IrO_2 into anodic TiO_2 nanotubes: a binary catalyst for electrochemical water splitting, *Int. J. Hydrog. Energy* 42 (2017) 6657–6664.
- [13] C. Li, J.-B. Baek, Recent advances in noble metal (Pt, Ru, and Ir)-based electrocatalysts for efficient hydrogen evolution reaction, *ACS Omega* 5 (2020) 31–40.

- [14] Y. Li, Y. Sun, Y. Qin, W. Zhang, L. Wang, M. Luo, H. Yang, S. Guo, Recent advances on water-splitting electrocatalysis mediated by noble-metal-based nanostructured materials, *Adv. Energy Mater.* 10 (2020), 1903120.
- [15] R. Gao, D. Yan, Recent development of Ni/Fe-based micro/nanostructures toward photo/electrochemical water oxidation, *Adv. Energy Mater.* 10 (2020), 1900954.
- [16] M. Arif, G. Yasina, L. Luo, W. Ye, M.A. Mushtaq, X. Fang, X. Xiang, S. Ji, D. Yan, Hierarchical hollow nanotubes of NiFeV-layered double hydroxides@CoVP heterostructures towards efficient, pH-universal electrocatalytic nitrogen reduction reaction to ammonia, *Appl. Catal. B: Environ.* 265 (2020), 118559.
- [17] R. Gao, J. Zhu, D. Yan, Transition metal-based layered double hydroxides for photo (electro)chemical water splitting: a mini review, *Nanoscale* 13 (2021) 13593–13603.
- [18] I. Hwang, I. Jang, G. Lee, Y. Tak, Binary cobalt and magnesium hydroxide catalyst for oxygen evolution reaction in alkaline water electrolysis, *Int. J. Electrochem. Sci.* 11 (2016) 6204–6214.
- [19] S. Anantharaj, S. Noda, Nickel selenides as pre-catalysts for electrochemical oxygen evolution reaction: a review, *Int. J. Hydrog. Energy* 45 (2020) 1576–15784.
- [20] L. Du, W. Du, H. Ren, N. Wang, Z. Yao, X. Shi, B. Zhang, J. Zaic, X. Qian, Honeycomb-like metallic nickel selenide nanosheet arrays as binder-free electrodes for high-performance hybrid asymmetric supercapacitors, *J. Mater. Chem. A* 5 (2017) 22527–22535.
- [21] K. Chandra, M. Yadav, Bimetallic chalcogenide nanocrystallites as efficient electrocatalyst for overall water splitting, *J. Alloy. Compd.* 852 (2021), 156736.
- [22] K. Zhang, Y. Li, S. Deng, S. Shen, Y. Zhang, G. Pan, Q. Xiong, Q. Liu, X. Xia, X. Wang, J. Tu, Molybdenum selenide electrocatalysts for electrochemical hydrogen evolution reaction, *Chem. Electro Chem.* 6 (2019) 3530–3548.
- [23] Y. Liu, H. Cheng, M. Lyu, S. Fan, Q. Liu, W. Zhang, Y. Zhi, C. Wang, C. Xiao, S. Wei, B. Ye, Y. Xie, Low overpotential in vacancy-rich ultrathin CoSe₂ nanosheets for water oxidation, *J. Am. Chem. Soc.* 136 (2014) 15670–15675.
- [24] K. Wang, Z. Lin, Y. Tang, Z. Tang, C.-L. Tao, D.-D. Qin, Y. Tian, Selenide/sulfide heterostructured NiCo₂Se₄/NiCoS₄ for oxygen evolution reaction, hydrogen evolution reaction, water splitting and Zn-air batteries, *Electrochim. Acta* 368 (2021), 137584.
- [25] S.M.N. Jeghan, G. Lee, One-dimensional hierarchical nanostructures of NiCo₂O₄, NiCo₂S₄ and NiCo₂Se₄ with superior electrocatalytic activities toward efficient oxygen evolution reaction, *Nanotechnology* 31 (2020), 295405.
- [26] L. Lv, Z. Li, Y. Ruan, Y. Chang, X. Ao, J.-G. Li, Z. Yang, C. Wang, Nickel-iron diselenide hollow nanoparticles with strongly hydrophilic surface for enhanced oxygen evolution reaction activity, *Electrochim. Acta* 286 (2018) 172–178.
- [27] X. Cao, E. Johnson, M. Nath, Expanding multinary selenide based high-efficiency oxygen evolution electrocatalysts through combinatorial electrodeposition: case study with Fe–Cu–Co selenides, *ACS Sustain. Chem. Eng.* 7 (2019) 9588–9600.
- [28] X. Xia, L. Wang, N. Sui, V.L. Colvill, W.W. Yu, Recent progress in transition metal selenide electrocatalysts for water splitting, *Nanoscale* 12 (2020) 12249–12262.
- [29] S. Anantharaj, E. Subhashini, K.C. Swaathini, T.S. Amarnath, S. Chatterjee, K. Karthick, S. Kundu, Respective influence of stoichiometry and NiOOH formation in hydrogen and oxygen evolution reactions of nickel selenides, *Appl. Surf. Sci.* 487 (2019) 1152–1158.
- [30] J. Zhu, Y. Ni, Phase-controlled synthesis and the phase dependent HER and OER performances of nickel selenide nanosheets prepared by an electrochemical deposition route, *Cryst. Eng. Comm.* 20 (2018) 3344–3352.
- [31] K.S. Bhat, H.S. Nagaraja, Nickel selenide nanostructures as an electrocatalyst for hydrogen evolution reaction, *Int. J. Hydrog. Energy* 43 (2018) 19851–19863.
- [32] H. Sun, J.-G. Li, L. Lv, Z. Li, X. Ao, C. Xu, X. Xue, G. Hong, C. Wang, Engineering hierarchical CoSe/NiFe layered-double-hydroxide nanoarrays as high efficient bifunctional electrocatalyst for overall water splitting, *J. Power Sources* 425 (2019) 138–146.
- [33] R. Yang, Y. Zhou, Y. Xing, D. Li, D. Jiang, M. Chen, W. Shi, S. Yuan, Synergistic coupling of CoFe-LDH arrays with NiFe-LDH nanosheet for highly efficient overall water splitting in alkaline media, *Appl. Catal. B* 253 (2019) 131–139.
- [34] B.W. Xue, C.H. Zhang, Y.Z. Wang, W.W. Xie, N.-W. Li, L. Yu, Recent progress of Ni-Fe layered double hydroxide and beyond towards electrochemical water splitting, *Nanoscale Adv.* 2 (2020) 5555–5566.
- [35] Y. Tang, Q. Liu, L. Dong, H.-B. Wu, X.-Y. Yu, Activating the hydrogen evolution and overall water splitting performance of NiFe LDH by cation doping and plasma reduction, *Appl. Catal. B* 266 (2020), 118627.
- [36] W. Liu, J. Bao, M. Guan, Y. Zhao, J. Lian, J. Qiu, L. Xu, Y. Huang, J. Qian, H. Li, Nickel-cobalt-layered double hydroxide nanosheet arrays on Ni foam as a bifunctional electrocatalyst for overall water splitting, *Dalton Trans.* 46 (2017) 8372–8376.
- [37] L. Feng, A. Li, Y. Li, J. Liu, L. Wang, L. Huang, Y. Wang, X. Ge, A highly active CoFe layered double hydroxide for water splitting, *Chem Chem* 82 (2017) 483–488.
- [38] J. Bao, Z. Wang, J. Xie, L. Xu, F. Lei, M. Guan, Y. Huang, Y. Zhao, J. Xia, H. Li, The CoMo-LDH ultrathin nanosheet as a highly active and bifunctional electrocatalyst for overall water splitting, *Inorg. Chem. Front.* 5 (2018) 2964–2970.
- [39] S.M.N. Jeghan, J. Kim, G. Lee, Hierarchically designed CoMo marigold flower-like 3D nano-heterostructure as an efficient electrocatalyst for oxygen and hydrogen evolution reactions, *Appl. Surf. Sci.* 546 (2021), 149072.
- [40] R. Zhao, Q. Li, X. Jiang, S. Huang, G. Fu, J.-M. Lee, Interface engineering in transition metal-based heterostructures for oxygen electrocatalysis, *Mater. Chem. Front.* 5 (2021) 1033–1059.
- [41] S. Wang, J. Wu, J. Yin, Q. Hu, D. Geng, L.-M. Liu, Improved electrocatalytic performance in overall water splitting with rational design of hierarchical Co₃O₄@NiFe layered double hydroxide core-shell nanostructure, *ChemElectroChem* 5 (2018) 1357–1363.
- [42] S. Dutta, A. Indra, Y. Feng, T. Song, U. Paik, Self-supported nickel iron layered double hydroxide-nickel selenide electrocatalyst for superior water splitting activity, *ACS Appl. Mater. Interfaces* 9 (2017) 33766–33774.
- [43] J. Zhou, L. Yu, Q. Zhu, C. Huang, Y. Yu, Defective and ultrathin NiFe LDH nanosheets decorated on V-doped Ni₃S₂ nanorod arrays: a 3D core-shell electrocatalyst for efficient water oxidation, *J. Mater. Chem. A* 7 (2019) 18118–18125.
- [44] J. Nie, M. Hong, X. Zhang, J. Huang, Q. Meng, C. Du, J. Chen, 3D amorphous NiFe LDH nanosheets electrodeposited on situ grown NiCoP@NC on nickel foam for remarkably enhanced OER electrocatalytic performance, *Dalton Trans.* 49 (2020) 4896–4903.
- [45] Y. Hu, W. Liu, K. Jiang, L. Xu, M. Guan, J. Bao, H. Ji, H. Li, Haynes, Constructing a CeO_{2-x}@CoFe-layered double hydroxide heterostructure as an improved electrocatalyst for highly efficient water oxidation, *Inorg. Chem. Front.* 7 (2020) 4461–4468.
- [46] Y. Wang, T. Wang, R. Zhang, Q. Liu, Y. Luo, G. Cui, S. Lu, J. Wang, Y. Ma, X. Sun, CuO @ CoFe layered double hydroxide core-shell heterostructure as an efficient water oxidation electrocatalyst under mild alkaline conditions, *Inorg. Chem.* 59 (2020) 9491–9495.
- [47] P.E. Blöchl, Projector augmented-wave method, *Phys. Rev. B* 50 (1994) 17953–17979.
- [48] G. Kresse, J. Hafner, Ab initio molecular dynamics for liquid metals, *Phys. Rev. B. Condens. Matter* 47 (1993) 558–561.
- [49] J.P. Perdew, K. Burke, M. Ernzerhof, Generalized gradient approximation made simple, *Phys. Rev. Lett.* 77 (1996) 3865–3868.
- [50] S.L. Dudarev, G.A. Botton, S.Y. Savrasov, C.J. Humphreys, A.P. Sutton, Electron-energy-loss spectra and the structural stability of nickel oxide: An LSDA+U study, *Phys. Rev. B* 57 (1998) 1505–1509.
- [51] M. Bajdich, M. García-Mota, A. Vojvodic, J.K. Nørskov, C.T. Campbell, Theoretical investigation of the activity of cobalt oxides for the electrochemical oxidation of water, *J. Am. Chem. Soc.* 135 (2013) 13521–13530.
- [52] N.J. Mosey, P. Liao, E.A. Carter, Rotationally invariant ab initio evaluation of Coulomb and exchange parameters for DFT+U calculations, *J. Chem. Phys.* 129 (2008) 14103.
- [53] W. Zhao, M. Bajdich, C. Spencer, A. Vojvodic, J.K. Nørskov, C.T. Campbell, Water dissociative adsorption on nio(111): energetics and structure of the hydroxylated surface, *ACS Catal.* 6 (2016) 7377–7384.
- [54] L. Wang, T. Maxisch, G. Ceder, Oxidation energies of transition metal oxides within the PBE+U framework, *Phys. Rev. B* 73 (2006), 195107.
- [55] A.A. Peterson, F. Abild-Pedersen, F. Studt, J. Rossmeisl, J.K. Nørskov, How copper catalyzes the electroreduction of carbon dioxide into hydrocarbon fuels, *Energy Environ. Sci.* 3 (2010) 1311–1315.
- [56] F. Dionigi, In-situ structure and catalytic mechanism of NiFe and CoFe layered double hydroxides during oxygen evolution, *Nat. Commun.* 11 (2020) 2522.
- [57] L. Wang, S.-M. Xu, X. Yang, S. He, S. Guan, G.I.N. Waterhouse, S. Zhou, Exploiting Co defects in CoFe-layered double hydroxide (CoFe-LDH) derivatives for highly efficient photothermal cancer therapy, *ACS Appl. Mater. Interfaces* 12 (2020) 54916–54926.
- [58] C. Hao, Y. Wu, Y. An, B. Cui, J. Lin, X. Li, D. Wang, M. Jiang, Z. Cheng, S. Hu, Interface-coupling of CoFe-LDH on MXene as high-performance oxygen evolution catalyst, *Mater. Today Energy* 12 (2019) 453–462.
- [59] Y. Rao, Y. Wang, H. Ning, P. Li, M. Wu, Hydrotalcite-like Ni(OH)₂ nanosheets in situ grown on nickel foam for overall water splitting, *ACS Appl. Mater. Interfaces* 8 (2016) 33601–33607.
- [60] Y. Liu, Q. Xu, R. Wang, Y. Zheng, L. Zhu, Z. Wang, W. Zheng, Ionothermal synthesis of three-dimensional hierarchical Ni₃Se₂ mesoporous nanosheet networks with enhanced performance for asymmetric supercapacitors, *J. Mater. Chem. A* 8 (2020) 797–809.
- [61] W. Yanyong, Z. Yiqiong, L. Zhijuan, X. Chao, F. Shi, L. Dongdong, S. Mingfei, W. Shuangyin, Layered double hydroxide nanosheets with multiple vacancies obtained by dry exfoliation as highly efficient oxygen evolution electrocatalysts, *Angew. Chem. Int. Ed.* 56 (2017) 1–6.
- [62] S.R. Ede, S. Anantharaj, K.T. Kumaran, S. Mishra, S. Kundu, One step synthesis of Ni(Ni(OH)₂) nanosheets (NSs) and their application in asymmetric supercapacitors, *RSC Adv.* 7 (2017) 5898–5911.
- [63] A. Sobhani, M. Salavati-Niasari, Synthesis and characterization of a nickel selenide series via a hydrothermal process, *Superlattices Micro* 65 (2014) 79–90.
- [64] H. Wu, X. Lu, G. Zheng, G.W. Ho, Topotactic engineering of ultrathin 2D nonlayered nickel selenides for full water electrolysis, *Adv. Energy Mater.* 8 (2018), 1702704.
- [65] J.-G. Li, H. Sun, L. Lv, Z. Li, X. Ao, C. Xu, Y. Li, C. Wang, Metal-organic framework-derived hierarchical (Co,Ni)Se₂@NiFe-LDH hollow nanocages for enhanced oxygen evolution, *ACS Appl. Mater. Interfaces* 11 (2019) 8106–8114.
- [66] D.S. Patil, S.A. Pawar, S.H. Lee, J.Ch Shin, CoFe layered double hydroxide for enhanced electrochemical performance, *J. Electroanal. Chem.* 862 (2020), 114012.
- [67] S.M.N. Jeghan, N. Kim, G. Lee, Mo-incorporated three-dimensional hierarchical ternary nickel-cobalt-molybdenum layer double hydroxide for high-efficiency water splitting, *Int. J. Hydrog. Energy* 46 (2021) 22463–22477.
- [68] B. Kirubasankar, V. Murugadoss, J. Lin, T. Ding, M. Dong, H. Liu, J. Zhang, T. Li, N. Wang, Z. Guo, S. Angaiah, In situ grown nickel selenide on graphene nanohybrid electrodes for high energy density asymmetric supercapacitors, *Nanoscale* 10 (2018) 20414–20425.
- [69] B. Singh, A. Indra, Tuning the properties of CoFe-layered double hydroxide by vanadium substitution for improved water splitting activity, *Dalton Trans.* 50 (2021) 2359–2363.

- [70] A.M.P. Sakita, R.D. Nocek, E. Vallés, A.V. Benedetti, Pulse electrodeposition of CoFe thin films covered with layered double hydroxides as a fast route to prepare enhanced catalysts for oxygen evolution reaction, *Appl. Surf. Sci.* 434 (2018) 1153–1160.
- [71] I. Barauskienė, E. Valatka, Layered nickel-cobalt oxide coatings on stainless steel as an electrocatalyst for oxygen evolution reaction, *Electrocatalysis* 10 (2019) 63–71.
- [72] A.T. Swesli, J. Masud, W.P.R. Liyanage, S. Umapathi, E. Bohannan, J. Medvedeva, M. Nath, Textured NiSe₂ film: Bifunctional electrocatalyst for full water splitting at remarkably low overpotential with high energy efficiency, *Sci. Rep.* 7 (2017) 2401.
- [73] R. Gao, D. Yan, Fast formation of single-unit-cell-thick and defect-rich layered double hydroxide nanosheets with highly enhanced oxygen evolution reaction for water splitting, *Nano Res.* 11 (2018) 1883–1894.
- [74] D. Xu, M.B. Stevens, Y. Rui, G. DeLuca, S.W. Boettcher, E. Reichmanis, Y. Li, Q. Zhang, H. Wang, The role of Cr doping in NiFe oxide/(oxy)hydroxide electrocatalysts for oxygen evolution, *Electrochim. Acta* 265 (2018) 10–18.
- [75] B.H.R. Suryanto, Y. Wang, R.K. Hocking, W. Adamson, C. Zhao, Overall electrochemical splitting of water at the heterogeneous interface of nickel and iron oxide, *Nat. Commun.* 10 (2019) 5599.
- [76] C. Zhu, D. Wen, S. Leubner, M. Oschatz, W. Liu, M. Holzschuh, F. Simon, S. Kaskel, A. Eychmüller, Nickel cobalt oxide hollow nanosponges as advanced electrocatalysts for the oxygen evolution reaction, *Chem. Commun.* 51 (2015) 7851–7854.
- [77] Y. Zhou, J. Hu, D. Li, Q. Gao, Single-layer CoFe hydroxides for efficient electrocatalytic oxygen evolution, *Chem. Commun.* 57 (2021) 7653–7656.
- [78] L. Wen, X. Zhang, J. Liu, X. Li, C. Xing, X. Lyu, W. Cai, W. Wang, Y. Li, Cr-Dopant induced breaking of scaling relations in CoFe layered double Hydroxides for improvement of oxygen evolution reaction, *Small* 15 (2019), 1902373.
- [79] V. Mehar, M. Kim, M. Shipilin, M.V. Bossche, J. Gustafson, L.R. Merte, U. Hejral, H. Grönbeck, E. Lundgren, A. Asthagiri, J.F. Weaver, Understanding the intrinsic surface reactivity of single-layer and multilayer PdO(101) on Pd(100), *ACS Catal.* 8 (2018) 8553–8567.
- [80] J.K. Nørskov, Electronic factors in catalysis, *Prog. Surf. Sci.* 38 (1991) 103–144.
- [81] B. Hammer, J.K. Nørskov, Why gold is the noblest of all the metals, *Nature* 376 (1995) 238–240.
- [82] X. Shen, Y. Pan, B. Liu, J. Yang, J. Zeng, Z. Peng, more accurate depiction of adsorption energy on transition metals using work function as one additional descriptor, *Phys. Chem. Chem. Phys.* 19 (2017) 12628–12632.
- [83] J. Li, P. Xu, R. Zhou, R. Li, L. Qiu, S.P. Jiang, D. Yuan, Co₉S₈-Ni₃S₂ heterointerfaced nanotubes on Ni foam as highly efficient and flexible bifunctional electrodes for water splitting, *Electrochim. Acta* 299 (2019) 152–162.
- [84] L. Yu, H. Zhou, J. Sun, F. Qin, F. Yu, J. Bao, Y. Yu, S. Chen, Z. Ren, Cu nanowires shelled with NiFe layered double hydroxide nanosheets as bifunctional electrocatalysts for overall water splitting, *Energy Environ. Sci.* 00 (2017) 1–3.
- [85] L. Yu, H. Zhou, J. Sun, F. Qin, D. Luo, L. Xie, F. Yu, J. Bao, Y. Li, Y. Yu, S. Chen, Z. Ren, Hierarchical Cu@CoFe layered double hydroxide core-shell nanoarchitectures as bifunctional electrocatalysts for efficient overall water splitting, *Nano Energy* 41 (2017) 327–336.
- [86] R. Gao, H. Zhanga, D. Yan, Iron diselenide nanoplatelets: Stable and efficient water-electrolysis catalysts, *Nano Energy* 31 (2017) 90–95.
- [87] W. Ye, Y. Yang, X. Fang, M. Arif, X. Chen, D. Yan, 2D cocrystallized metal–organic nanosheet array as an efficient and stable bifunctional electrocatalyst for overall water splitting, *ACS Sustain. Chem. Eng.* 7 (2019) 18085–18092.
- [88] M. Arif, G. Yasin, M. Shakeel, M.A. Mushtaq, W.Y. X. Fang, S. Ji, D. Yan, Highly active sites of NiVB nanoparticles dispersed onto graphene nanosheets towards efficient and pH-universal overall water splitting, *58* (2021) 237–246.
- [89] L. Ya, N. Zhang, Y. Wang, Y. Nia, D. Yan, C. Hua, Facile formation of 2D Co₂P@Co₃O₄ microspheres through in-situ topotactic conversion and surface corrosion: Bifunctional electrocatalysts towards overall water splitting, *J. Power Sources* 374 (2018) 142–148.